Summer 6-20-2022

Differentiating Fissure-Fed Lava Flow Types and Facies Using RADAR and LiDAR: An Example from the 2014–2015 Holuhraun Lava Flow-field

Gavin Douglas Tolometti
Western University, gtolomet@uwo.ca

Catherine D. Neish
Western University, cneish@uwo.ca

Christopher W. Hamilton
Lunar and Planetary Laboratory, University of Arizona

Gordon R. Osinski
Western University, gosinski@uwo.ca

Antero Kukko
Centre of Excellence in Laser Scanning Research, Finnish Geospatial Research Institute

See next page for additional authors

Citation of this paper:
Tolometti, G. D., Neish, C. D., Hamilton, C. W., Osinski, G. R., Kukko, A., & Voigt, J. R. C. Differentiating Fissure-Fed Lava Flow Types and Facies Using RADAR and LiDAR: An Example from the 2014–2015 Holuhraun Lava Flow-field. *Journal of Geophysical Research: Solid Earth*, e2021JB023419.

Authors
Gavin Douglas Tolometti, Catherine D. Neish, Christopher W. Hamilton, Gordon R. Osinski, Antero Kukko, and Joana R.C. Voigt

Differentiating Fissure-Fed Lava Flow Types and Facies Using RADAR and LiDAR: An Example from the 2014–2015 Holuhraun Lava Flow-field

G. D. Tolometti[1,2], C. D. Neish[1,2], C. W. Hamilton[3], G. R. Osinski[1,2], A. Kukko[4], J. R. C. Voigt[3].

[1]*Department of Earth Sciences, University of Western Ontario, London, ON, N6A 3K7, Canada*

[2]*Institute for Earth and Space Exploration, University of Western Ontario, London, ON, N6A 3K7, Canada*

[3]*Lunar and Planetary Laboratory, University of Arizona, Tucson, AZ, 85718, USA*

[4]*Centre of Excellence in Laser Scanning Research, Finnish Geospatial Research Institute, Masala, 02430, Finland*

Abstract

Distinguishing between lava types and facies using remote sensing data is important for interpreting the emplacement history of lava flow-fields on Earth and other planetary bodies. Lava facies typically include a mixture of lava types and record the collective emplacement history of material preserved at a particular location. We seek to determine if lava facies in the 2014–2015 Holuhraun lava flow-field are discernable using radar roughness analysis. Furthermore, we also seek to distinguish between lava types using high resolution Light Detection and Ranging (LiDAR) data. We extracted circular polarization ratios (CPR) from the Uninhabited Aerial Vehicle Synthetic Aperture Radar and cross-polarization (VH/VV) data from the Sentinel-1 satellite to analyze the surface roughness of three previously mapped lava facies: rubbly, spiny, and undifferentiated rubbly–spiny. Using the Kruskal-Wallis test, we reveal that all but one pair of the facies are statistically separable. However, the populations overlap by 88–89% for CPR and 64–67% for VH/VV. Therefore, owing to large sample populations ($n > 2 \times 10^5$), slight differences in radar data may be used to probabilistically infer the presence of a particular facies, but not directly map them. We also calculated the root-mean-square slope and Hurst exponents of five different lava types using LiDAR topography (5 cm/pixel). Our results show minute differences between most of the lava types, with the exception of the rubbly pāhoehoe, which is discernable at 1σ. In brief, the presence of "transitional" lava types (e.g., rubbly pāhoehoe) within fissure-fed lava flow-fields complicates remote sensing-based mapping.

Plain Language Summary

The characteristics of geologically recent lava flow-fields inform our understanding magmatic and volcanic processes on Earth and other planetary bodies. Fissure-fed lava flow-fields, like the 2014–2015 Holuhraun lava flow-field in Iceland, include “transitional” surface textures formed from the disruption of solidified crusts. The resulting lava types form in multiple stages, which modify and mix the surfaces, making them challenging to map. At reasonable scales (e.g., 1:800), mappable units, or “facies”, include a mixture of lava types. Field observations may be used to identify lava types within such facies, but in remote, inaccessible locations on Earth, and on the surface of other planetary bodies, we can only rely on using data collected from orbiting spacecraft. We seek to determine if lava facies and lava types can be differentiated using radar and LiDAR data. We find we cannot differentiate the major lava facies using radar data, and few lava types can be discerned using decimetre-scale LiDAR topography data. The surface characteristics of the lava flow-field are therefore complex, and it is important to recognize the limitations of automated techniques for mapping the distribution of materials within fissure-fed lava flow fields on Earth and other planets using solely radar and LiDAR.

1 Introduction

The study of large fissure-fed lava flow-fields contributes to our understanding of the emplacement mechanisms of flood lavas (1–100 km^3 Dense Rock Equivalent (DRE)) and flood basalts (>100 km^3 DRE), which have modified the surface and global climate of Earth and other planetary bodies (Duraiswami et al., 2008; Guilbaud et al., 2005; Keszthelyi et al., 2006; Self et al., 2006; Thordarson & Larsen, 2007; Wilson & Head, 1994; Zimbelman, 1998). The 2014–2015 Holuhraun lava flow-field in Iceland is important as an exceptional terrestrial analogue for fissure-fed eruption products on other planetary bodies (Bonnefoy et al., 2019; Bonny et al., 2018; Dirscherl & Rossi, 2018; Hamilton, 2015; Kolzenburg et al., 2018; Kolzenburg et al., 2017; Pedersen et al., 2017).

The 2014–2015 Holuhraun lava flow-field consists of eight different lava facies (Voigt et al., 2021a). These lava facies were mapped at a scale of 1:800 based on their albedo, texture, and morphology. However, ground-truthing revealed that the facies are composed of a mixture of lava flow types. Lava flows are most commonly subdivided into pāhoehoe, ‘a‘ā, and block lava types (MacDonald, 1953); however, there exist a broader range of “transitional” lava types formed through episodic or continuous fragmentation of solidified lava crusts, such as rubbly pāhoehoe, which are typically associated with fissure-fed eruptions (e.g., Hamilton, 2019; Harris et al., 2017; Kilburn, 2000; Rowland & Walker, 1990; Solana et al., 2004; Thordarson & Larsen, 2007; Voigt et al., 2021a, 2021b). These transitional lava types commonly co-occur at a fine scale (on the order of meters or less), which makes mapping the spatial distribution of these materials challenging at a reasonable digitizing scale (e.g., 1:800). Consequently, we refer to facies when attempting to subdivide lava flow-fields into geomorphological classes. For simplicity, we name the facies after the dominant lava flow type they contain, but acknowledge that these are typically mixed classes that also include a wider range of lava flow types. The mixed nature of transitional lava facies greatly complicates automated mapping methods using remote sensing data and poses challenges in terms of interpretation related to the geological process. This is because transitional lava types (e.g., rubbly pāhoehoe and spiny pāhoehoe) include materials formed at different times due to successive episodes of crustal formation, disruption, and transport prior to their final emplacement. Ideally, we would map the spatial distribution of unmixed lava types, but since this is not possible at reasonable mapping scales for an entire flow-field we must instead map facies and acknowledge the complexities that arise from mapping units that include a mixture of lava types.

We investigate whether the lava facies and lava types within the 2014–2015 Holuhraun lava flow-field can be separated by analyzing their surface roughness using radar and LiDAR-derived topography data. Surface roughness is defined as a measure of the variation in topography at scales of a few metres or less, and has been quantified using a variety of field and remote sensing techniques, including 1-D profile measurements (e.g., Campbell and Shepard, 1996; Shepard et al., 2001), synthetic aperture radar (e.g., Campbell and Shepard, 1996; Neish et al., 2017; Tolometti et al., 2020), and high-resolution topography data (Fan et al., 2018; Morris et al., 2008; Rodriguez Sanchez-Vahamonde & Neish, 2021; Voigt, et al., 2021c; Whelley et al., 2017; Zanetti et al., 2018). We are interested in investigating surface roughness in this work because it can be related to eruption and lava emplacement mechanisms (Duraiswami et al., 2008, 2014; Griffiths & Fink, 1992; Guilbaud et al., 2005; Harris et al., 2017; Kilburn, 2000; Rowland & Walker, 1990; Voigt et al., 2021b) and has important implications for remote sensing studies of planetary surfaces, such as volcanic terrains on Venus and Mars.

We utilize polarimetric radar remote sensing data in this work to determine if the Holuhraun lava facies can be separated using their observed scattering characteristics (e.g., Carter et al., 2011; Neish et al., 2017; Neish & Carter, 2014). Quad-polarized Uninhabited Aerial Vehicle Synthetic Aperture Radar (UAVSAR) L-band (λ = 24 cm) (Rosen et al., 2006) and dual-polarized Sentinel-1 C-band (λ = 5.6 cm) (Torres et al., 2012) radar data are available for the entire surface of the Holuhraun lava flow-field, providing the opportunity to analyze surface roughness at two different wavelengths. To complement our radar analyses, we also seek to determine if the lava types within a given lava facies can be differentiated using high-resolution topography data. To discern between lava types, we calculate roughness statistics from centimetre-scale digital elevation models (DEMs), converted from dense point clouds acquired from a kinematic LiDAR system. These investigations help to explore the geomorphological complexity of lava flow-fields and determine the limits of automated mapping methods for fissure-fed lavas, which include transitional lava types.

1.1. Geologic Setting

The 2014–2015 Holuhraun lava flow-field (Figure 1) is situated within the northern part of the Bárðarbunga–Veiðivötn volcanic system and it was the largest effusive basaltic eruption in Iceland since the 1783–1785 Laki eruption (Thordarson & Self, 1993). Volcanic unrest associated with this eruption began on August 15th, 2014, when minor seismic swarm activity was detected beneath the northeastern flank of the Bárðarbunga volcano (Bonnefoy et al., 2019; Coppola et al., 2017; Dirscherl & Rossi, 2018; Gudmundsson et al., 2016; Hjartardóttir et al., 2016; Pedersen et al., 2017; Sigmundsson et al., 2015). The seismic swarm propagated 48 km along a lineament to the northeast and terminated in a floodplain 8 km north of the Dyngjujökull outlet glacier (Bonnefoy et al., 2019; Gudmundsson et al., 2016). On August 29th, 2014, a small fissure erupted for ~4 hours (Pedersen et al., 2017). Following a hiatus of two days the new fissure opened further north, initiating an effusive basaltic eruption that extended from August 31st, 2014, to February 27th, 2015. By the end of the eruption, a total estimated dense rock equivalent (DRE) volume (assuming mean bulk lava void space of 15 to 20%) of 1.2 ± 0.1 km^3 (Bonny et al., 2018) had erupted onto the floodplain, covering an area of ~83.82 km^2 (Voigt, Hamilton, Scheidt, et al., 2021).

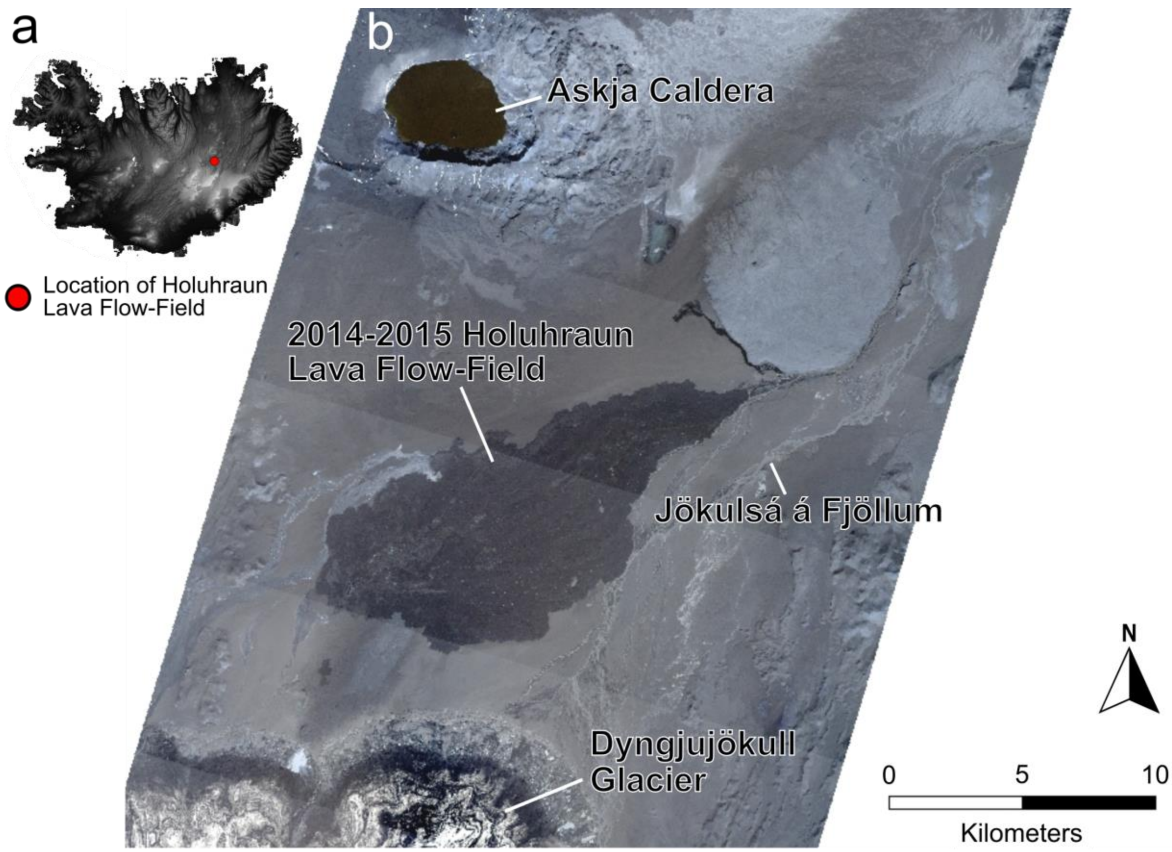

Figure 1. Location of the Holuhraun lava flow-field in central Iceland. (a) ArcticDEM hillshade image of Iceland at 1 km/pixel scale shows the location of the lava flow-field (red point). The ArcticDEM data was acquired from the National Geospatial-Intelligence Agency (NGA)–National Science Foundations (NSF) Initiative. (b) Mosaic of six RGB images (3 m/pixel)

collected by the PlanetScope satellite constellation of the Holuhraun lava flow-field between the Askja Caldera and the Dyngjujökull glacier. The Dover CubeSats in the PlanetScope constellation are operated by Planet (Planet Team, 2017) and the RGB images were collected on August 21st, 2020.

The Holuhraun lava flow-field includes eight facies, which were mapped using high-resolution aerial images and field observations (Voigt et al., 2021a). These facies and their percentage of the total flow-field area are as follows: rubbly (57.35%), spiny (25.96%), undifferentiated rubbly–spiny (9.59%), shelly (5.58%), pāhoehoe (1.24%), flat-lying knobby (0.58%), vent-proximal edifice (0.19%), and channel interior (0.16%). The name for each facies refers to the dominant lava type or volcanic structure that is present within each domain. For example, the dominant lava type in the rubbly facies is rubbly pāhoehoe, but the unit also includes minor exposure of other related lava types.

In this study, we evaluate the hypothesis that polarimetric radar can differentiate the three dominant facies units in the Holuhraun lava flow-field: rubbly, spiny, and undifferentiated rubbly–spiny. Together, these three facies cover ~93% of the lava flow-field and, therefore, they record most of the information about the lava flow-field's emplacement history. The remainder of the facies cover areas that are too small for the extraction of statistically reliable polarimetric radar values.

Previous work by Voigt et al. (2021b) discussed the challenges in distinguishing between lava facies using 0.05 to 0.5 m/pixel DEMs generated using stereo-photogrammetry. Their approach involved quantifying the surface roughness of the lava facies using root-mean-square

(RMS) slope and Hurst exponent (H) to determine the statistical separability of the units. They emphasized that it is challenging to characterize lava facies using these data because transitional lava types (e.g., rubbly pāhoehoe and spiny pāhoehoe) are not uniquely resolvable in high-resolution topographic data when examined at a practical mapping scale (i.e., 1:800). Here, we consider the problem using radar measurements and LiDAR-derived DEMs to determine if additional information can be gleaned by examining these alternative data sets.

2 Materials and Methods

2.1. Field-based Approaches

Due to the difficulty of transporting heavy LiDAR systems over treacherous lava flow surfaces, we focused on field-based investigations on four lava types: rubbly pāhoehoe, spiny pāhoehoe, shelly pāhoehoe, and pāhoehoe (Figure 2a–d). We also examined the subtype of spiny pāhoehoe, which includes polygonal plates (Figure 2e). Similar platy morphologies have been identified in the 1960 Kaphoho eruption Hawaiʻi (Rowland & Walker, 1987), the 1783–1784 Laki eruption in Iceland (Keszthelyi et al., 2000), and in association with platy-ridged lava flows on Mars (Keszthelyi et al., 2004).

Rubbly pāhoehoe is a transitional lava type (Harris et al., 2017; Keszthelyi et al., 2004; Tolometti et al., 2020) formed by the mechanical fracturing of a solidified crust, rather than the viscous tearing of fluidal lava at high shear strain rates (Figure 2a). Spiny pāhoehoe is another transitional lava type with surfaces that are rough at the millimetre and centimetre-scale with elongate spines oriented parallel to the local flow direction. Along the margins of the lava flow-field, spiny pāhoehoe units are expressed as a network of coalesced and inflated lobes and toes (Figure 2b). The shelly pāhoehoe (Jones, 1943) lava type is associated with a partially drained and deflated lava pond in the vent-proximal region and its surface texture is similar to that of the spiny pāhoehoe (Figure 2c; Voigt et al., 2021a). However, beneath the thin (<10-cm-thick) crust, shelly pāhoehoe includes void space formed by the evacuation of lava and/or gas from the flow interior. The pāhoehoe lava type exhibits lobate to sheet-like morphologies with coherent surface crusts that exhibit ropes, wrinkles, and billows (Figure 2d).

Lastly, we examined a subset of the spiny pāhoehoe lava type that exhibits a platy surface. These units are typically associated with inflation plateaus with the plates exhibiting wave-like structures formed by successive extrusions of viscous lava prior to disruption into plates (Voigt et al., 2021a). The platy surfaces exhibit spinose textures, with spines oriented perpendicular to the front of the lava waves. The plates are bounded by extensional fractures, which commonly exhibit extrusions (i.e., squeeze-ups) of jagged and viscous lava as well compressional ridges composed of disrupted and imbricated slabs of a once coherent spiny pāhoehoe crust (Figure 2e). Within the inflation plateaus that exhibit a platy surface, we also documented circular and elliptical lava-rise pits (Figure 2f). For simplicity, we distinguish spiny pāhoehoe units with platy surfaces as platy lava, but these are effectively the same as the "toothpaste" lava units described by Rowland & Walker (1987) and Harris et al. (2017).

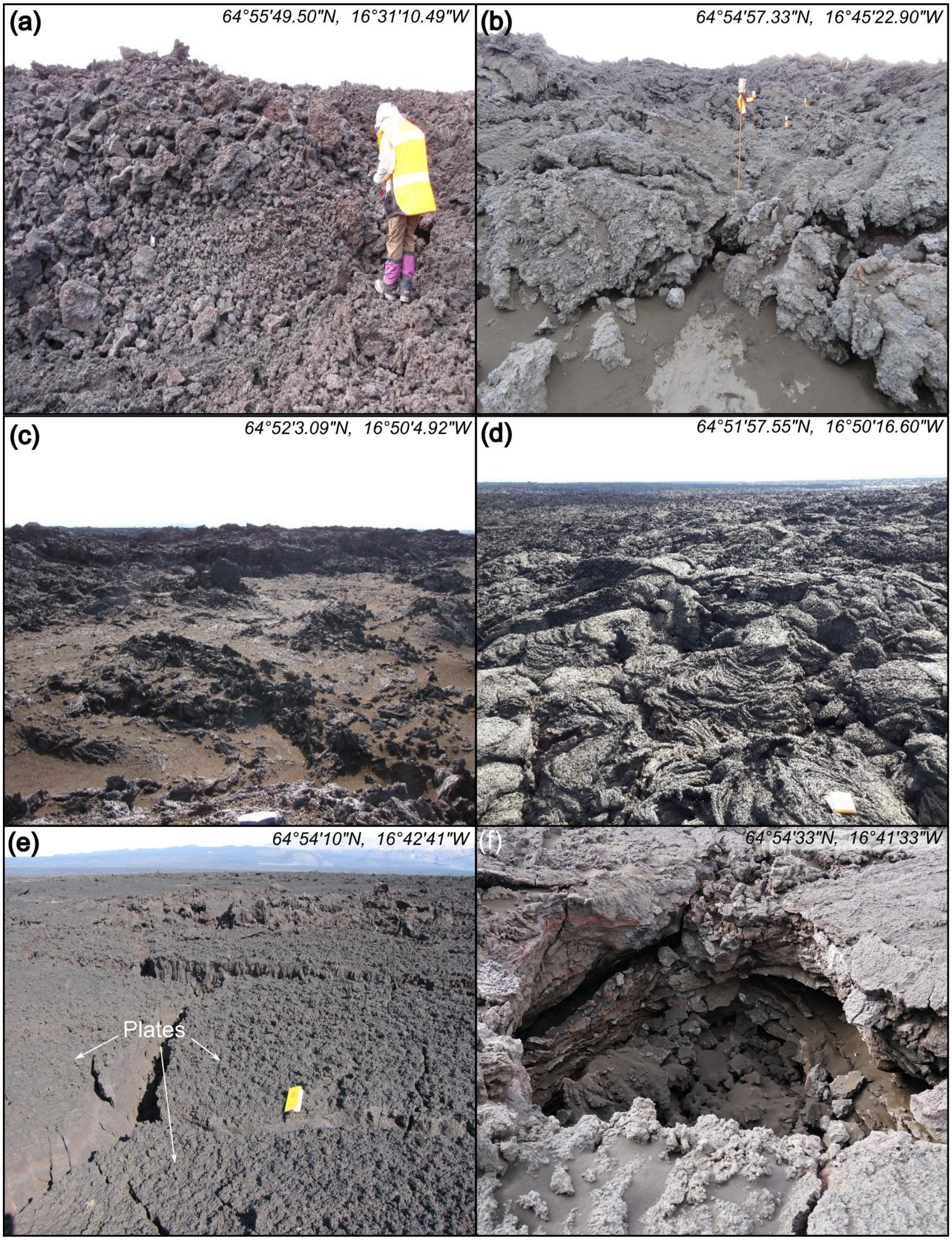

Figure 2. The lava types and morphological subsets studied at Holuhraun. (a) Rubbly pāhoehoe lava type with centimetre to decimetre-scale fragments of a once coherent crust. Some fragments

exhibit block-shapes. For scale, the person in image is ~1.7-m-tall. (b) Spiny pāhoehoe lobe with toes along its margins. For scale, the walking path marker is ~1-m-tall. (c) Shelly pāhoehoe with a fragile spiny pāhoehoe-like crust near the eastern margin of the vent. For scale, the field notebook is approximately 15 cm × 9 cm. (d) Pāhoehoe lava with a hummocky and lobate morphology along the east and south margins of the vent. Field notebook appears for scale. (e) Platy lava within the inflation plateaus in the medial of the spiny facies. Plates are separated by extrusions of toothpaste lava squeeze-ups and ridges formed by compressional bucking of the slabby pāhoehoe crust. The field notebook appears for scale. (f) A lava-rise pits located within the platy spiny pāhoehoe unit.

2.2. Radar Processing

2.2.1. UAVSAR Quad-Polarized L-Band Radar

To analyze the surface roughness of the rubbly, spiny, and undifferentiated rubbly–spiny facies, we calculated the circular polarization ratio (CPR) (Figure 3) from radar data acquired by the quad-polarized L-band (λ = 24 cm) UAVSAR airbourne platform operated by the Jet Propulsion Laboratory (JPL) (Rosen et al., 2006). Orthorectified UAVSAR data products were downloaded from the JPL UAVSAR site (https://uavsar.jpl.nasa.gov), and CPR was calculated using methods outlined in Campbell (2002), Neish et al., (2017), and Zebker & Lou (1990) (see Data Repository). Observations were obtained on May 30th, 2015, on flights 15083 DT 4 and DT 5. CPR is defined as the ratio of the same-sense circular (SC) polarization of the transmitted radar signal to the opposite-sense circular (OC) polarization of the transmitted signal (Campbell, 2002). Smooth surfaces (e.g., lava ponds) typically return a greater OC than SC backscatter because of their single-bounce, mirror-like reflections that flip the polarization of the transmitted signals. This produces low CPR values (<0.5). Rough surfaces (e.g., ‘a‘ā clinker) scatter signals in multiple directions, returning approximately equal SC and OC signals (diffuse scattering). Rough surfaces typically produce CPR values that approach one (0.5–1.0). The CPR may exceed unity when signals reflect off rock edges, cracks, or natural corner reflectors (e.g., polyhedral blocks with smooth facets). This produces a double-bounce backscatter effect, which flips the polarization twice and thus increases the SC backscatter (Campbell, 2012). We only used CPR from the UAVSAR data because CPR is a strong parameter for representing surface roughness and provides more information about radar scattering properties than same and opposite-sense linear polarization data alone (e,g., Carter et al., 2011; Neish & Carter, 2014). The quality and validity of UAVSAR radar data has been tested by numerous other workers, demonstrating that the high signal-to-noise ratio is effective for studying the radar scattering properties of different surfaces on Earth (Fore et al., 2015; Minchew et al., 2012).

2.2.2. Sentinel-1 Dual-Polarized C-Band Radar

In addition to L-band CPR data, we analyzed the lava facies surface roughness using C-band (λ = 5.6 cm) dual-polarized radar data acquired by the European Space Agency (ESA) Sentinel-1 satellite (Torres et al., 2012). To quantify the surface roughness of the lava facies, we calculated the linear polarization ratio VH/VV (e.g., Campbell, 2002; Campbell and Shepard, 1996) as VH and VV backscatter datasets were available at the highest spatial resolution, 10 m/pixel. We processed Level-1 Ground Range Detected (GRD) Sentinel-1 data using the freely available SeNtinel Application Program (SNAP) developed by ESA. The GRD products consist of multi-looked SAR images that were projected to ground range using the Earth ellipsoid model WGS84. We used SNAP radiometric calibration tools to convert the amplitude and phase of the returned radar signals to VH and VV backscatter values (Figure 4a and b) and the VH/VV ratio (Figure 4c).

2.3. Extracting and Analyzing Radar Data

Following the steps to produce CPR (Figure 3) and VH/VV images (Figure 3c), we reduced the radar speckle noise using a 3 × 3 low-pass filter, increasing the number of looks per pixel from 9 to 81 (Tolometti et al., 2020). After the low-pass filter was applied, we extracted the mean CPR and VH/VV of the rubbly, spiny, and undifferentiated rubbly–spiny facies using polygons delimited by Voigt et al. (2021a). These polygons are freely accessible as an ArcGIS geodatabase from the University of Arizona Campus Repository (Voigt & Hamilton, 2021).

We excluded all CPR data extracted from the westernmost part of the UAVSAR data set (Flight 15083 D5) (i.e., west of the image seam in Figure 3) because it has an incidence angle >65°. This is approximately 10° greater than the maximum incidence angle in the easternmost part of the UAVSAR data set (Flight 15083 DT 4), which covers the majority of the lava flow-field. CPR increases with increasing incidence angle (Campbell, 2002; Carter et al., 2004); and, therefore, these CPR are not comparable to the CPR in the other part of the UAVSAR observation. The Sentinel-1 radar data are not influenced by significant differences in incidence angle because of the greater altitude of the orbiter compared to the low-altitude flying UAVSAR platform. We therefore restricted our analysis to the rubbly, spiny, and undifferentiated rubbly–spiny facies in the main body of the lava flow-field (medial and distal), east of the image seam in Figure 3 to facilitate the comparison between the dual and quad-polarized radar results.

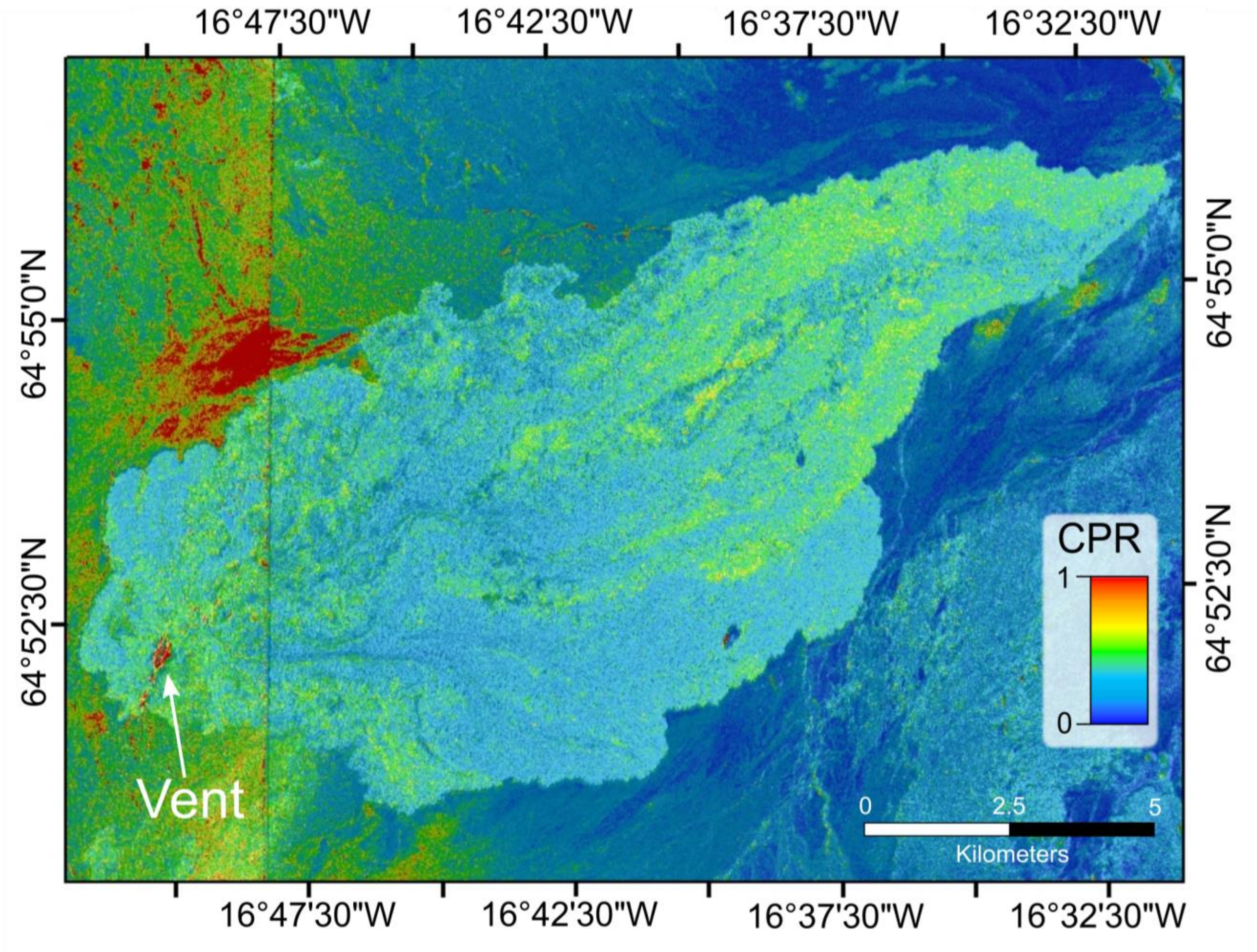

Figure 3. A circular polarization ratio (CPR) image (5 m/pixel) overlaid on a total backscatter image of the Holuhraun lava flow-field calculated from polarimetric radar data acquired by the UAVSAR airbourne platform. The CPR image is a mosaic of two UAVSAR flight swaths collected in May 2015 (ID: PolSAR: Flight 15083 (2015-05-30), DT 4, v1 (main body of lava flow-field) and PolSAR: Flight 15083 (2015-05-30), DT 5, v1 (vent of lava flow-field). The speckle noise was reduced in the image by applying a low-pass filter, increasing the number of looks from 9 to 81. Note that the image on the left is east-looking, and the image on the right is west-looking. As a result, the highest incidence angles are near the image seam (N–S oriented line east of the vent).

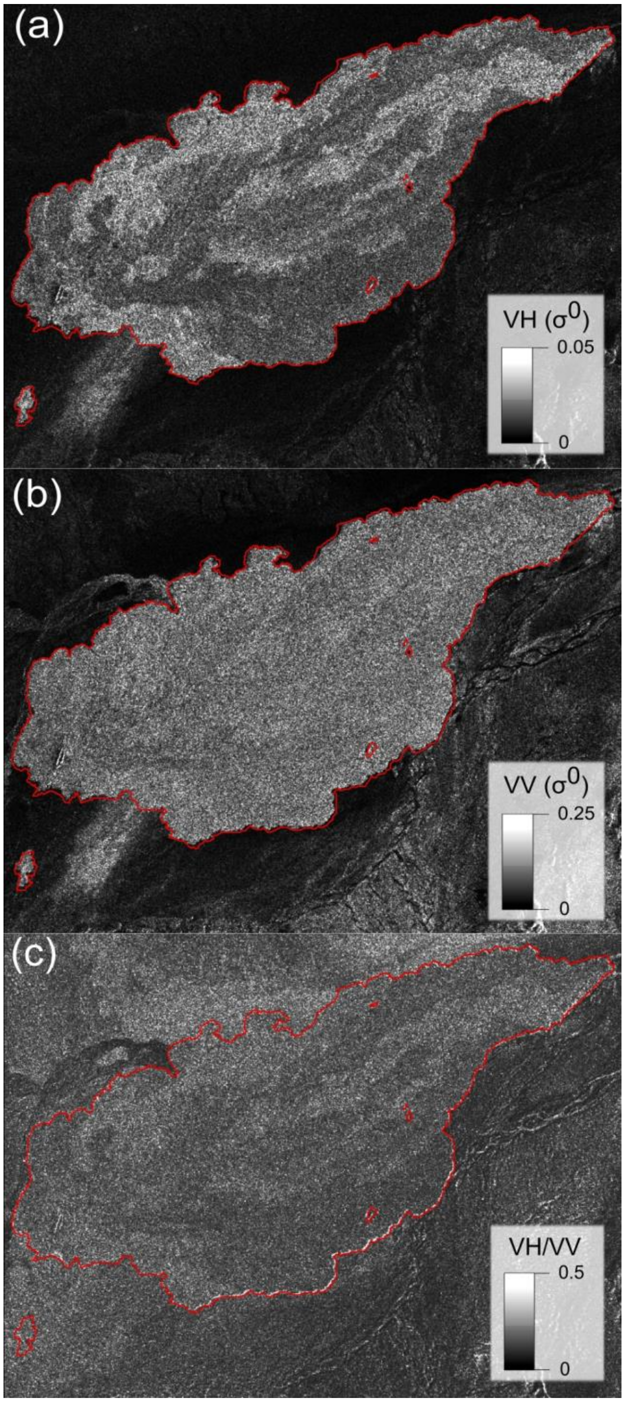

Figure 4. Dual-polarization Sentinel-1 C-band radar image of the Holuhraun lava flow-field (outlined in red). The Sentinel-1 data was acquired on August 6th, 2019, and was processed by ESA (ID S1B_IW_GRDH_1SDV_20190806T073250_20190806T073315_017462_020D76_0DA9) on

August 31st, 2019 (Copernicus Sentinel data 2015). The data were downloaded as Ground Range Detection products and were calibrated using ESA's SNAP software. Image is set to a WGS84/UTM Zone 28 projection, centered at 65°12'14°N; 17°56'45°W, and has a 10 m/pixel resolution. (a) Image of the σ^0_{VH} polarization data. (b) Image of the σ^0_{VV} polarization data. (c) VH/VV ($\sigma^0_{VH}/\sigma^0_{VV}$) ratio image.

In addition to quantifying CPR and VH/VV of the rubbly, spiny, and undifferentiated rubbly–spiny facies, we produced two polarimetric radar threshold maps comprising different data ranges. The threshold maps were created to see if the lava facies could be distinguished qualitatively. We subdivided the CPR and VH/VV data into five ranges (0–0.2, 0.2–0.4, 0.4–0.6, 0.6–0.8, and 0.8 to >1.0). The low-pass filter was insufficient to remove enough speckle noise for data thresholding, and so to further reduce the speckle noise in the SAR data, we applied an Enhanced Lee filter using the Image Analysis Speckle Function tool in ESRI ArcGIS before setting the above thresholds. The Enhanced Lee Filter reduces speckle noise while minimizing the loss of radiometric and textural characteristics in the radar images (Lee & Pottier, 2018). We set the filter size to 9 × 9 pixels because it marks the point at which the reduction in speckle noise with increasing pixel averaging levels out. If we increased the number of looks beyond this, speckle noise would not have reduced significantly, and we would begin to lose radiometric and textural characteristics in the data (Lee & Pottier, 2018; López-Martínez & Fàbregas, 2008).

2.4. Topographic Data

High-resolution 3D topographic LiDAR data was collected using the AKHKA-R4DW kinematic dual-wavelength laser scanning system (Kukko et al., 2020). The kinematic LiDAR system collected dense point clouds from ~50 m × ~50 m areas covering the surfaces of different lava types. Surfaces were scanned using Riegl VUX-1HA that illuminates a target with a laser at 1017 kHz pulse frequency and 250 lines/second, measuring ground range values with an accuracy of 5 mm. The scanner operates at a wavelength of 1550 nm. A second laser scanner, a Riegl miniVUX-1UAV, was used in conjunction with the primary scanner, operating at a wavelength of 905 nm and providing 100 kHz pulse frequency and 100 lines/second. Both laser scanners have a 360° Field of View (FoV) and were used to map surrounding areas in cross-track scanning with a 30-degree angle between the two scan planes. A Labybug5+ panoramic camera (FLIR systems, Inc., USA) synchronously captured image data. NovAtel Pwrpak7 Global Navigation Satellite System (GNSS) receiver and antenna attached to the instrument provided absolute global positioning in the field based on Global Positioning System (GPS) and a space-based GLObal NAvigation Satellite System (GLONASS) constellation satellites aided with a stationary Trimble R10 base station for differential processing. Sensor orientation and short-term dynamics are captured with ISA-100C near navigation grade inertial measurement unit, data of which is fused in tightly coupled processing of the system trajectory (Waypoint Inertial Explorer, NovAtel Inc., Canada). Point cloud spatial resolution within 20 m of the scanner is on the order of 5 mm (depending on distance from the scanner), with vertical accuracy <2 cm and absolute global position <10 cm. After raw data calibration and processing using Riegl RiProcess and RiPrecision software modules (RIEGL Laser Measurement Systems GmbH, Austria), the point clouds were converted into digital elevation models (DEM) using ESRI ArcGIS. The maximum resolution set for the DEMs in this work was set to 5 cm/pixel, equal to the maximum resolution of the stereo-derived DTMs used by Voigt et al. (2021b) to analyze the topographic roughness of the Holuhraun lava facies. The high precision and accuracy of the kinematic LiDAR system (see Kukko et al., (2020) for details) and high spatial resolution of the point clouds will reduce uncertainties in our roughness statistic calculations.

Metre-scale topography for the lava facies also includes ArcticDEM topography data. ArcticDEM data was acquired from a National Geospatial-Intelligence Agency (NGA)–National Science Foundations (NSF) initiative and constructed from in-track and cross-track high-resolution (0.5 m/pixel) images acquired from the DigitalGlobe constellation satellites (WorldView-1, WorldView-2, WorldView-3, and GeoEye-1 optical imaging satellites). Vertical accuracy of ArcticDEM data, calculated from ICESat point clouds, is –1 cm to 7 cm (Candela et al., 2017). We downloaded a 2 m/pixel (4 m accuracy in horizontal and vertical planes) topography data tile that covers the entire Holuhraun lava flow-field from the NGA ArcticDEM Web Map database (https://www.pgc.umn.edu/data/arcticdem/), produced on July 22nd, 2018 (ID: 16_54_2m_reg_dem).

2.4.1. Topographic Roughness Statistics

To extract topographic roughness statistics from the LiDAR and ArcticDEM topography data, we calculated the RMS slope and the Hurst exponent (*H*), which are parameters recommended by Shepard et al. (2001) for surface roughness characterization. The RMS slope is described as the standard deviation of slopes about a mean along a set profile (Shepard et al., 2001). The *H* value describes how roughness changes with increasing scale, and ranges from 0 to 1. When *H* approaches 0, it indicates that the surface roughness changes as the scale increases, becoming either smoother or rougher. If *H* approaches 1, it indicates that the surface roughness remains unchanged with an increase in scale. A *H* of 0.5 is termed Brownian since Brownian motion will produce this type of surface (Shepard et al., 2001).

We calculated the RMS slope using the Allan variance (v^2) (Equation 1), which samples the topographic profile (z_i) at every interval step (Δx).

$$v^2(\Delta x) = \frac{1}{n}\sum_{i=1}^{n}[z(x_i) - z(x_i + \Delta x)]^2$$

Equation 1

The variable *n* represents the number of sample points in the topographic profile (examples are shown in Figure 5), and $z(x_i)$ is the height of the surface at point x_i. Using values from Equation 1, we calculate RMS slope using Equation 2,

$$RMS_{slope} = \frac{v(\Delta x)}{\Delta x}$$

Equation 2

We calculated *H* using Equation 3 where Δx_0 is the horizontal reference scale (Figure 6). For some surfaces, one *H* value is not enough to describe roughness. Breakpoints can occur when the roughness transitions from one *H* value to another (Figure 6), assumed to represent different processes that either produced or modified the surface (Shepard et al., 2001).

$$v(\Delta x) = RMS_{slope}\left(\frac{\Delta x}{\Delta x_0}\right)^H$$

Equation 3

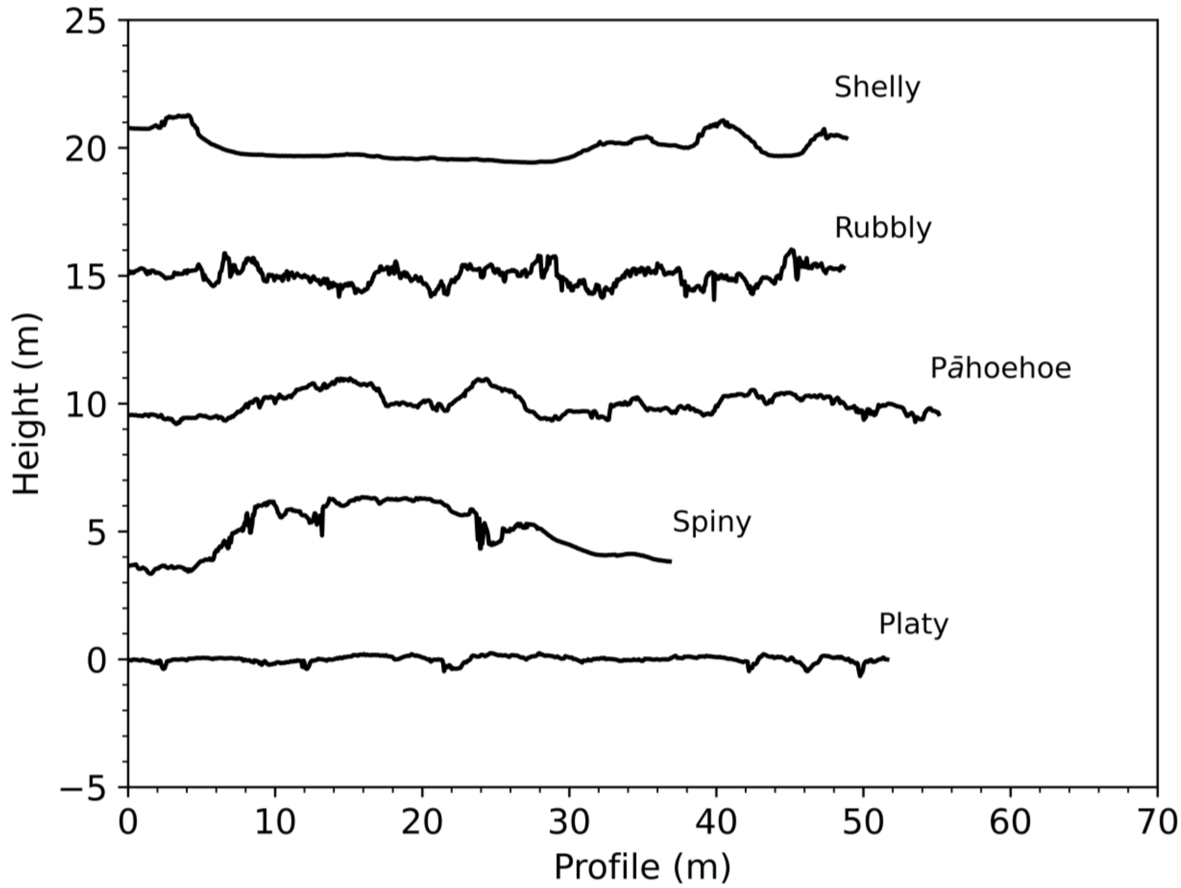

Figure 5. Example topographic profiles of the four Holuhraun lava types and a platy subset of the spiny pāhoehoe lava type, which exhibits a plate-ridged surface with extensional zones and toothpaste-like lava squeeze-ups. The profiles were extracted from LiDAR derived DEMs with a horizontal resolution of 5 cm/pixel. A best-fit line was removed from the profile, to correct for any regional slope. Each profile is offset by 5 m to prevent data overlap. The topographic profiles were extracted from the following LiDAR Data (see Table 2 in Section 3.2): 20190801_1_c (Shelly), 20190803_1_a (Rubbly), 20190805_1_a (Pāhoehoe), 20190729_2_d (Spiny), and 20190803_1_c (Platy).

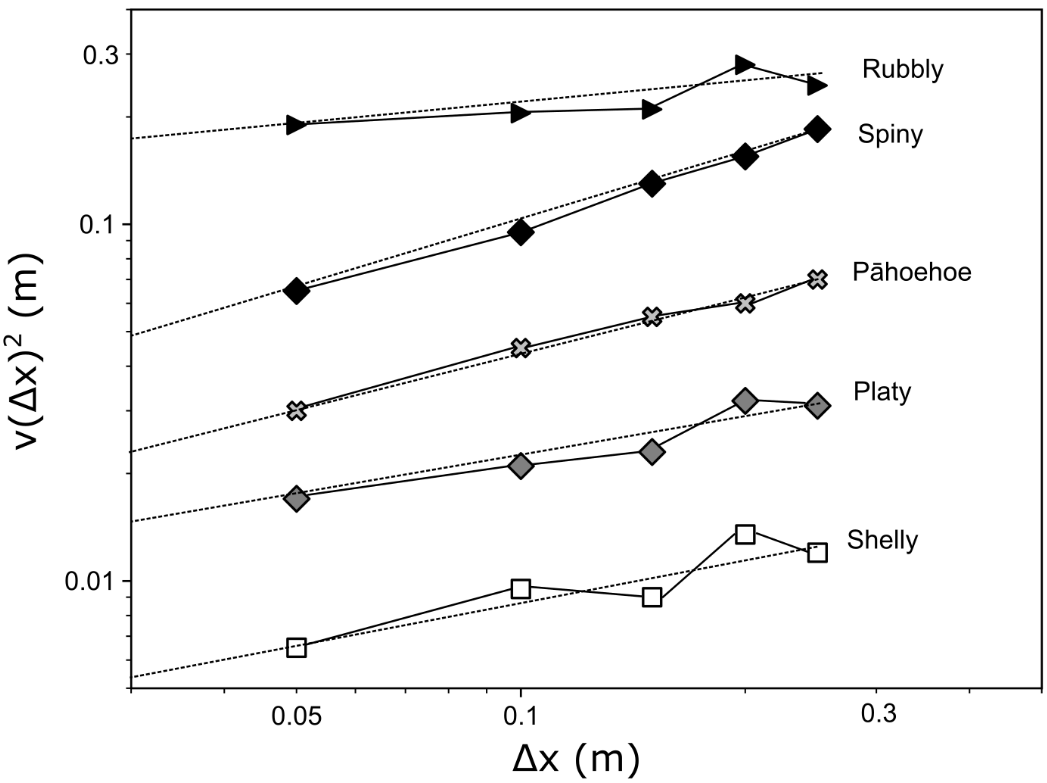

Figure 6. Example variograms of the four Holuhraun lava types and a platy subset of spiny pāhoehoe are plotted using data from the topographic profiles shown in Figure 5. Points are plotted every 5 cm between 5 cm and 25 cm. *H* is the slope of the line and the RMS slope is related to the *y*-intercept of the variogram. The dashed lines represent the calculated best fit line for each lava flow type variogram example. Outlier data point in the rubbly example not connected to line of best fit.

Three profile lengths were selected to incorporate a range of surface roughness measurements at different scales (centimetre-scale, decimetre-scale, and metre-scale). The first profile length was set at 2.5 m to obtain roughness statistics over a 0.05 m to 0.25 m reference scale with step intervals of 0.05 m. The second profile length was set at 20 m to obtain roughness statistics over a 0.25 m to 2 m reference scale with step intervals of 0.25 m. The third profile length, which was only applied to the metre-scale ArcticDEM data, was set at 100 m to obtain roughness statistics over a 2 m to 12 m reference scale with step intervals of 2 m. We adhered to the recommendations by Shepard et al. (2001) that the profile length should be approximately 10 times the size of the largest value in the set reference scale. Both the second and third reference scales have been used by other workers to study the surface roughness and topography of lava flows and impact melt flows on terrestrial planetary bodies (e.g., Campbell and Shepard, 1996; Neish et al., 2017; Rodriguez Sanchez-Vahamonde and Neish, 2021; Shepard et al., 2001).

We extracted 2.5 m long profiles (for centimetre-scale roughness) and 20 m long profiles (for decimetre-scale roughness) along the lava surfaces in the LiDAR DEMs, and 100 m long profiles (for metre-scale roughness) along the lava facies in the ArcticDEM data in 2-D perpendicular directions (across and along flow). We detrended each profile by removing the best-fit linear function from the data, calculated the Allan variance, and derived the RMS slope and H. This process was repeated with the starting point on the DEM increasing by one pixel until we reached the edge of the region. In this way, each pixel along a row become the center of a profile and was assigned the derived RMS slope and H value. We extracted the mean and standard deviation of the RMS slope and H distributions are each lava type using the zonal statistics tool in ESRI ArcGIS.

3 Results

3.1. Surface Roughness Inferred from Radar Backscatter

We obtained the mean and standard deviation of CPR and VH/VV ($\frac{\sigma^0 VH}{\sigma^0 VV}$) from each lava facies using traced polygons, except for the polygons proximal to the vent, where radar incidence angles are too high for broad comparisons across the lava flow-field. The results (Figure 7a) show that all three facies return moderate CPR values, with the spiny facies returning the lowest mean CPR overall . The spiny facies returned a CPR value of 0.45 ± 0.08 at 1 standard deviation (σ), the rubbly facies a CPR value of 0.47 ± 0.1 at 1 σ, and the undifferentiated rubbly-spiny facies a CPR value of 0.47 ± 0.09 at 1 σ. From the Sentinel-1 C-band VH/VV data (Figure 7b), the rubbly and undifferentiated rubbly–spiny facies returned similar values (Figure 7b). The rubbly facies have a mean VH/VV of 0.17 ± 0.11 at 1 σ, the undifferentiated rubbly–spiny facies are characterized by a mean VH/VV of 0.18 ± 0.13 at 1 σ, and the spiny facies have a mean VH/VV of 0.21 ± 0.11 at 1 σ.

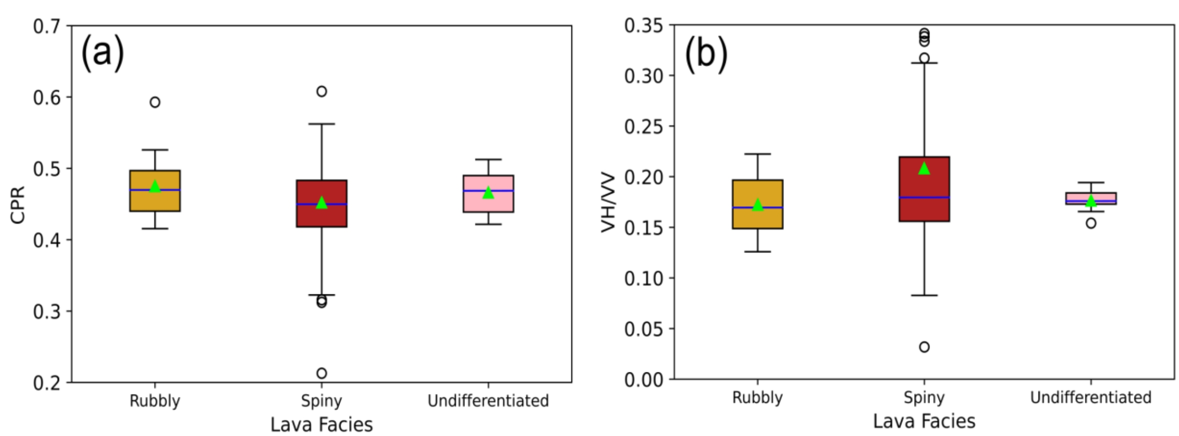

Figure 7. Statistical distribution of radar data means extracted from each discrete polygon representing rubbly (n = 15), spiny (n = 68), and undifferentiated rubbly–spiny (n = 7) facies .

The boxplots show the mean (green triangle), median (dark blue line), interquartile range (IRQ), which spans 50% of data (coloured box showing the lower and upper quartile at the base and top), maximum (upper quartile + 1.5 × IQR) and minimum (lower quartile – 1.5 × IQR) values (whisker lines), and outliers above and below the ±62.5 percentile, respectively (white circles). (a) L-band CPR mean value from each lava facies polygon. (b) C-band VH/VV mean value from each lava facies polygon.

To further test whether there is a statistical significance between radar values associated with the three facies , we examined all data values extracted from the lava facies polygons (Figure 8a and b): rubbly (n = 1,048,575), spiny (n = 551.598), and undifferentiated rubbly–spiny (n = 225,676). All three populations are not normally distributed and so we applied the Kruskal–Wallis test to determine if the medians of two or more Non-Gaussian groups are separable. Kruskal–Wallis test results (Table 1) show that only the undifferentiated rubbly–spiny and spiny facies under VH/VV data are not statistically separable from one another. However, despite the test revealing all lava facies are statistically separable under CPR and almost all under VH/VV, there frequency distributions significantly overlap (Figure 8c and d). For instance, all CPR populations overlap by >88% and all VH/VV data distributions overlap by >64% (Figure 8e and f). In other words, given large sample sizes ($n > 2 \times 10^5$), subtle differences in the frequency distribution of radar values may be used to probabilistically infer the occurrence of a facies based on slight differences between population medians. However, the value of any given sample cannot be used to reliably determine its facies identity because the radar data populations are too overlapping to provide a unique mapping between a sample and the correct facies. Thus, while the Kruskal–Wallis test shows that most transitional lava faces are statistically separable given a large enough sample size, the strongly overlapping radar data populations prohibit deterministic facies assignments from individual samples, or observations, thereby complicating direct mapping of the spatial distribution of lava facies within a lava flow-field using radar data alone.

Table 1

Summary of Kruskal Wallis test. Lava facies are statistically separable if returned p-value is <0.05. Y – Yes, statistically separable. N – not statistically separable.

Lava Facies Comparison	CPR		Separable	VH/VV		Separable
	H-Stat	p		H-Stat	p	
Rubbly vs. Spiny	49368.31	~0	Y	23426.62	~0	Y
Rubbly vs. Undiff.	10368.67	~0	Y	7998.37	~0	Y
Spiny vs. Undiff.	3374.75	~0	Y	2.92	0.09	N

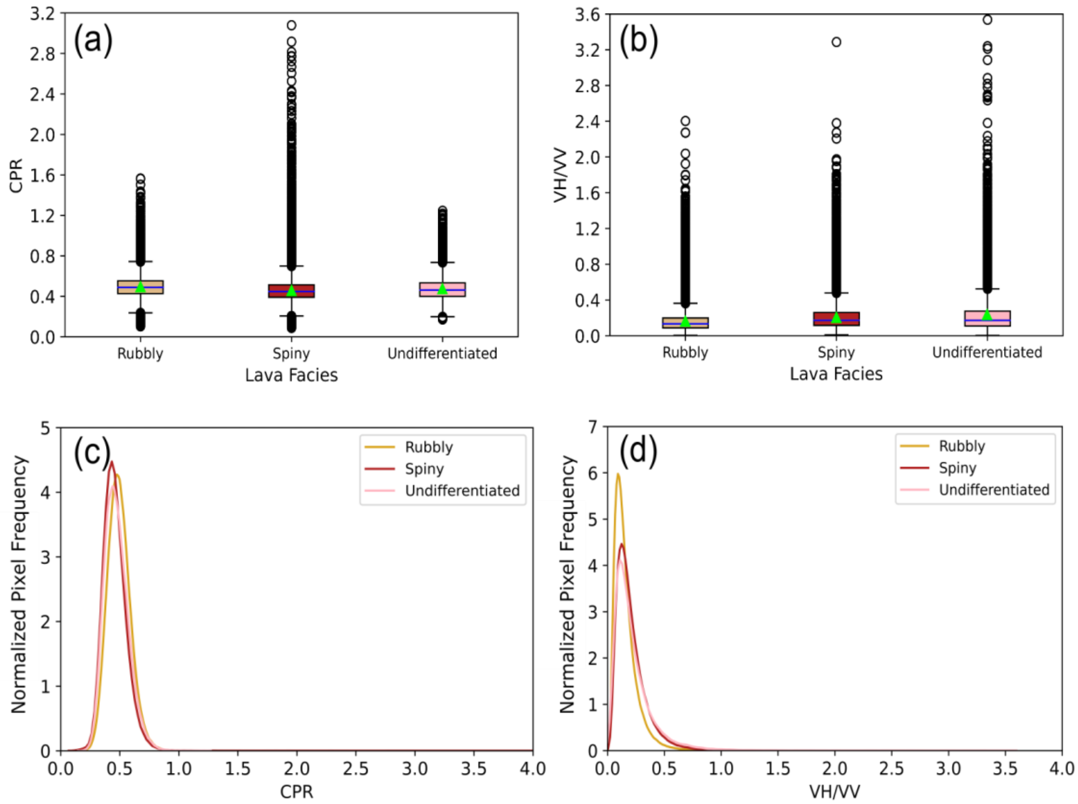

(e)

CPR

	Rubbly	Spiny	Undiff.
Rubbly	1.00	0.88	0.89
Spiny	0.88	1.00	0.88
Undiff.	0.89	0.88	1.00

(f)

VH/VV

	Rubbly	Spiny	Undiff.
Rubbly	1.00	0.67	0.65
Spiny	0.67	1.00	0.64
Undiff.	0.65	0.64	1.00

Figure 8. Statistical analysis of 2014–2015 Holuhraun lava facies L-band CPR and C-band VH/VV data. Boxplots (a – CPR, b – VH/VV) show the distribution of radar data within each traced lava facies polygon. The boxplots show the mean (green triangle), median (dark blue line), interquartile range (IRQ), which spans 50% of data (coloured box showing the lower and upper quartile at the base and top), maximum (upper quartile + 1.5 × IQR) and minimum (lower quartile – 1.5 × IQR) values (whisker lines), and outliers above and below the ±62.5 percentile, respectively (white circles). Normalized frequency distributions of the total population of (c) CPR and (d) VH/VV data extracted from all lava facies polygons. The frequency distributions of

CPR and VH/VV data revealing Non-Gaussian distributions for the rubbly (n = 1048575), spiny (n = 551598), and undifferentiated rubbly–spiny (n = 225676) facies populations; and Comparison between the faction of population overlap (in %) between the three facies using the (e) CPR and (f) VH/VV data.

In the CPR threshold map (Figure 9a), we observe subtle differences between CPR values in the rubbly and spiny facies. In the northeastern and northwestern regions of the lava flow - field, the rubbly facies have a marginally greater CPR (Figure 9b), standing out from the spiny facies that also covers a large portion of these regions (Figure 9c). The rubbly facies locally exhibit areas with CPR ranging from 0.6–0.8, whereas the spiny facies CPR are consistently less than 0.6. In the central and southern regions, however, the rubbly facies have a lower CPR than the spiny facies (Figure 9c). The undifferentiated rubbly–spiny facies are more challenging to discern since it returns CPR similar to the rubbly facies (Figure 9d). The VH/VV threshold map (Figure 10a) shows remarkably similar patterns, with the rubbly and spiny facies showing slight differences (Figures 10b–c). A major difference is that the undifferentiated rubbly–spiny facies are more comparable to the spiny facies than the rubbly facies (see Figures 10c–d).

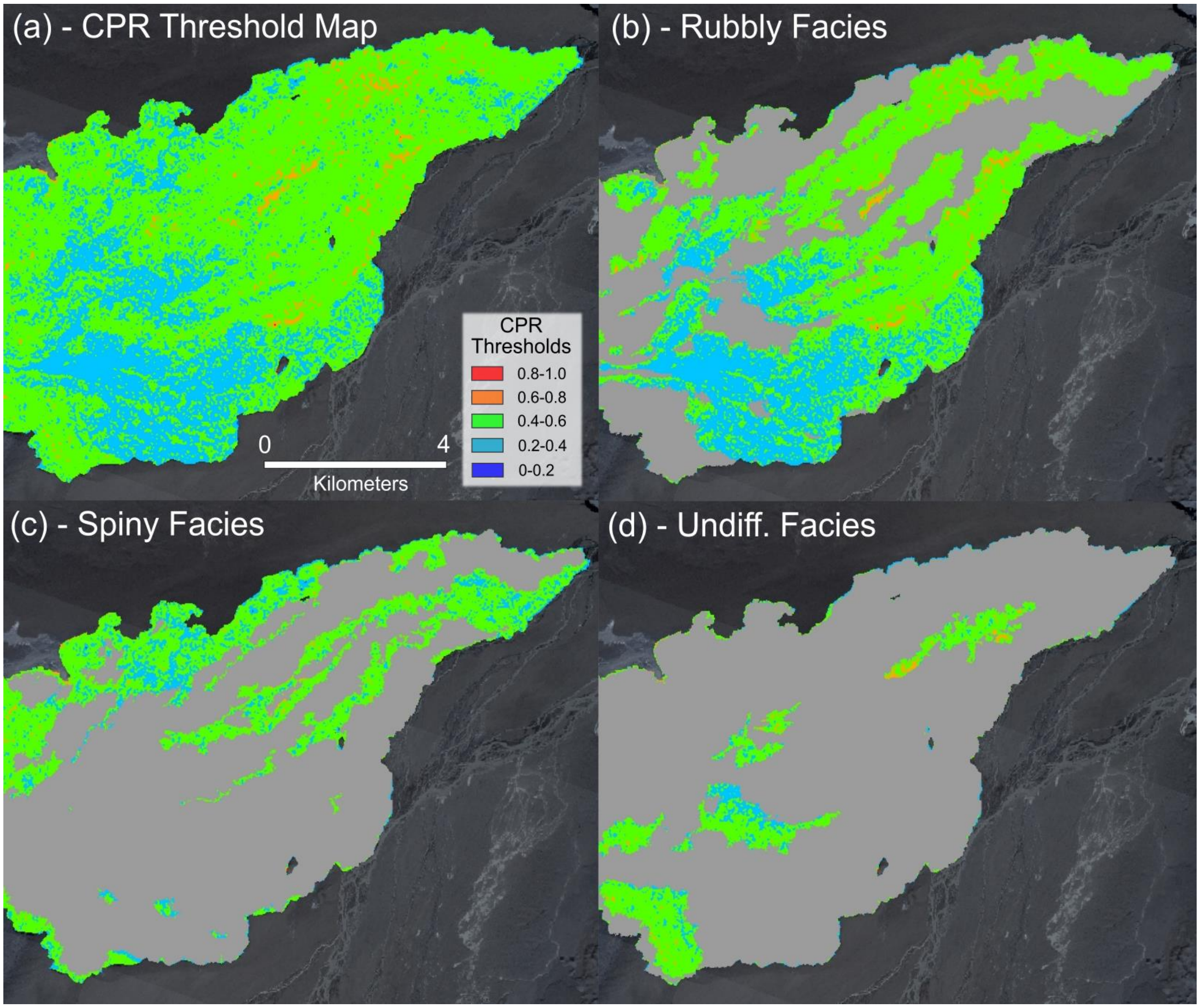

Figure 9. A threshold map of the UAVSAR CPR data overlaid with the lava facies polygons from Voigt and Hamilton (2021). In (b–d), each of the three main facies are highlighted to reveal their CPR values (colourized at 0.2 intervals), while the other facies are grayed out. (a) CPR threshold map of the 2014–2015 Holuhraun lava flow-field produced by applying a 9 × 9 Enhanced Lee filter to the CPR data. Vent region is not included in this image due to the greater incidence angles of the UAVSAR observation. (b) Rubbly facies in the CPR threshold map. (c) Spiny facies in the CPR threshold map. (d) Undifferentiated rubbly–spiny facies in the CPR threshold map.

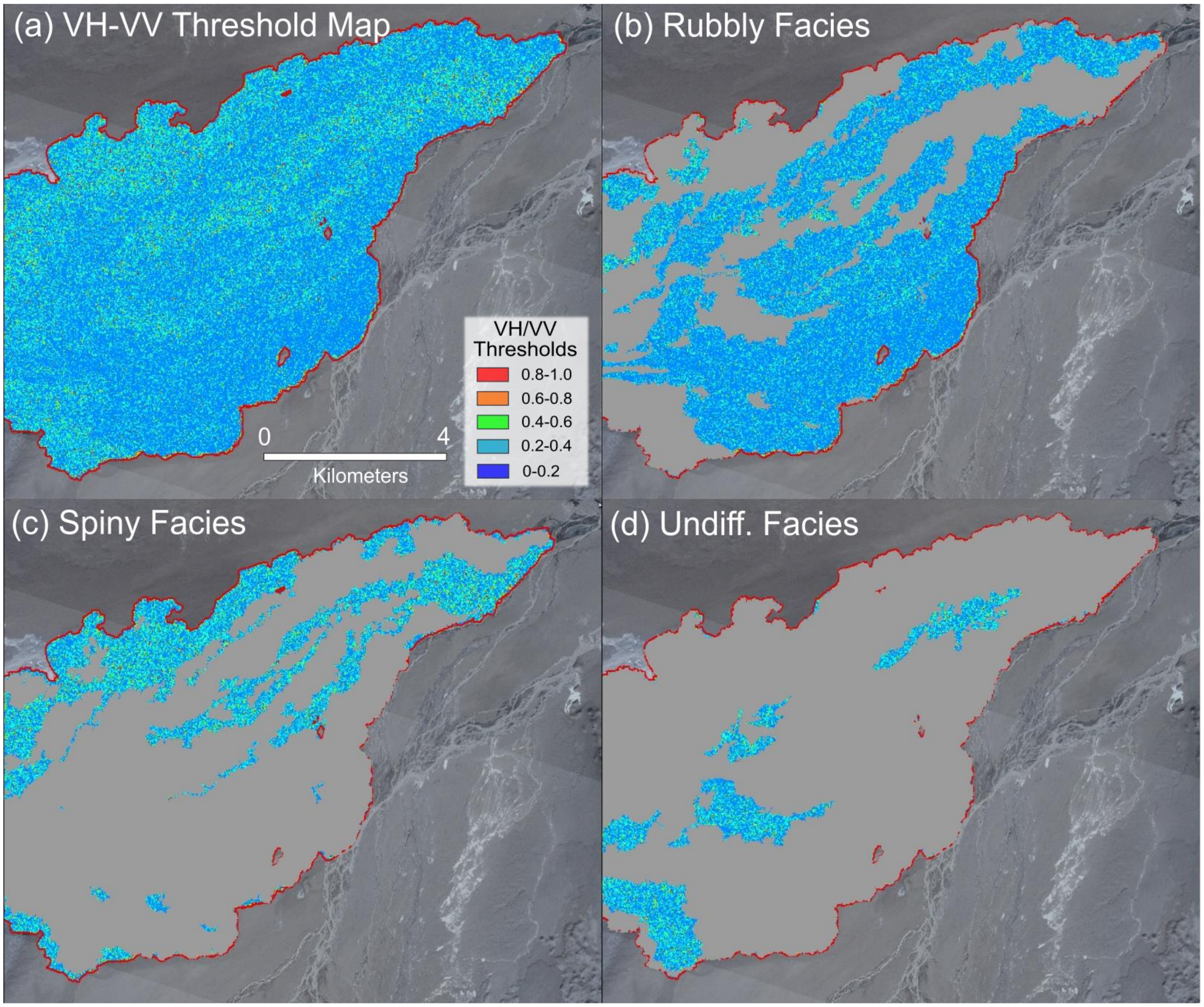

Figure 10. A threshold map of VH/VV calculated from Sentinel-1 $\sigma°_{VH}$ and $\sigma°_{VV}$ data overlaid with the lava facies polygons from Voigt and Hamilton (2021). In (b–d), each of the three main facies are highlighted to reveal their VH/VV values (colourized at 0.2 intervals), while the other facies are grayed out. (a) VH/VV threshold map of the 2014–2015 Holuhraun lava flow-field produced by applying a 9 × 9 Enhanced Lee filter to the VH/VV data. Vent region is not included to make the comparison with the UAVASAR CPR threshold map. (b) Rubbly facies in the VH/VV threshold map. (c) Spiny facies in the VH/VV threshold map. (d) Undifferentiated rubbly–spiny facies in the VH/VV threshold map.

3.2. Topographic Surface Roughness

To further characterize the surface topography and roughness of lava types that comprise the 1:800-scale facies map units, we collected a total of twenty-five LiDAR scans in the field, sixteen of which were located within the spiny facies, including thirteen examples of platy lava and three examples of spiny pāhoehoe; three were located in the pāhoehoe facies; two were located in the shelly facies, and four were located in the rubbly facies. Using LiDAR to enable fine-scale mapping, we were able to identify specific locations within each of these facies that included unmixed lava types.

We collected more examples of platy and spiny lava because these lava types were easier to access and traverse in the field. Examples of the lava flow type DEMs and roughness statistic raster's generated from the LiDAR data are presented in Figure 11 (a–e). The roughness data collected from the LiDAR scans were calculated at 0.05–0.25 m (profile length, 2.5 m and Δx, 0.05 m) and 0.25–2 m reference scales (profile length, 20 m and Δx, 0.25 m) (Table 2). We were only able to extract RMS slopes and H values from one rubbly pāhoehoe surface at the decimetre-scale because three of the four LiDAR scans had dimensions less than double the profile length (20 m). This lava type is unstable and difficult to traverse on foot, especially with the kinematic LiDAR system.

At the centimetre-scale (0.05–0.25 m), the lava types have RMS slope values from 4.78° to 16.70° and H from 0.13 to 0.6 (Figure 12). The three pāhoehoe examples were moderately rough, with RMS slope values from 10.29° ± 2.04° to 10.70° ± 1.83° and H from 0.38 to 0.49 (Figure 12). The high RMS slope values for the pāhoehoe was likely a result of the centimetre-scale surface features such as the ropy billows, wrinkles, and sharp spinose textures. The two shelly pāhoehoe examples have lower RMS slope values compared to the pāhoehoe lava type, 5.27° ± 0.95° and 6.35° ± 1.25°, and both exhibit H of 0.44 (Figure 12). The rubbly pāhoehoe lava type has the greatest RMS slope, 16.70° ± 3.67°, owing to the size of the fragments on its disrupted crustal surface. It also returned the greatest variation in H, 0.29 to 0.6 (Figure 12). The platy lava has the greatest variation in RMS slope values and the smoothest surface at the centimetre-scale (RMS slope, 4.78° ± 1.05° to 11.56° ± 3.88° and H, 0.13 to 0.39) (Figure 12). The three spiny pāhoehoe lava types with lobe and toe features (Figure 12) along the western margin of the lava flow-field have RMS slopes ranging from 7.90° ± 1.51° to 11.52° ± 2.86°, and H values from 0.2 to 0.36. In general, it is difficult to discriminate between the lava types using the RMS slope and H values. However, the rubbly pāhoehoe does stand out as having the highest values of RMS slope and H at a reference scale of 0.05–0.25 m.

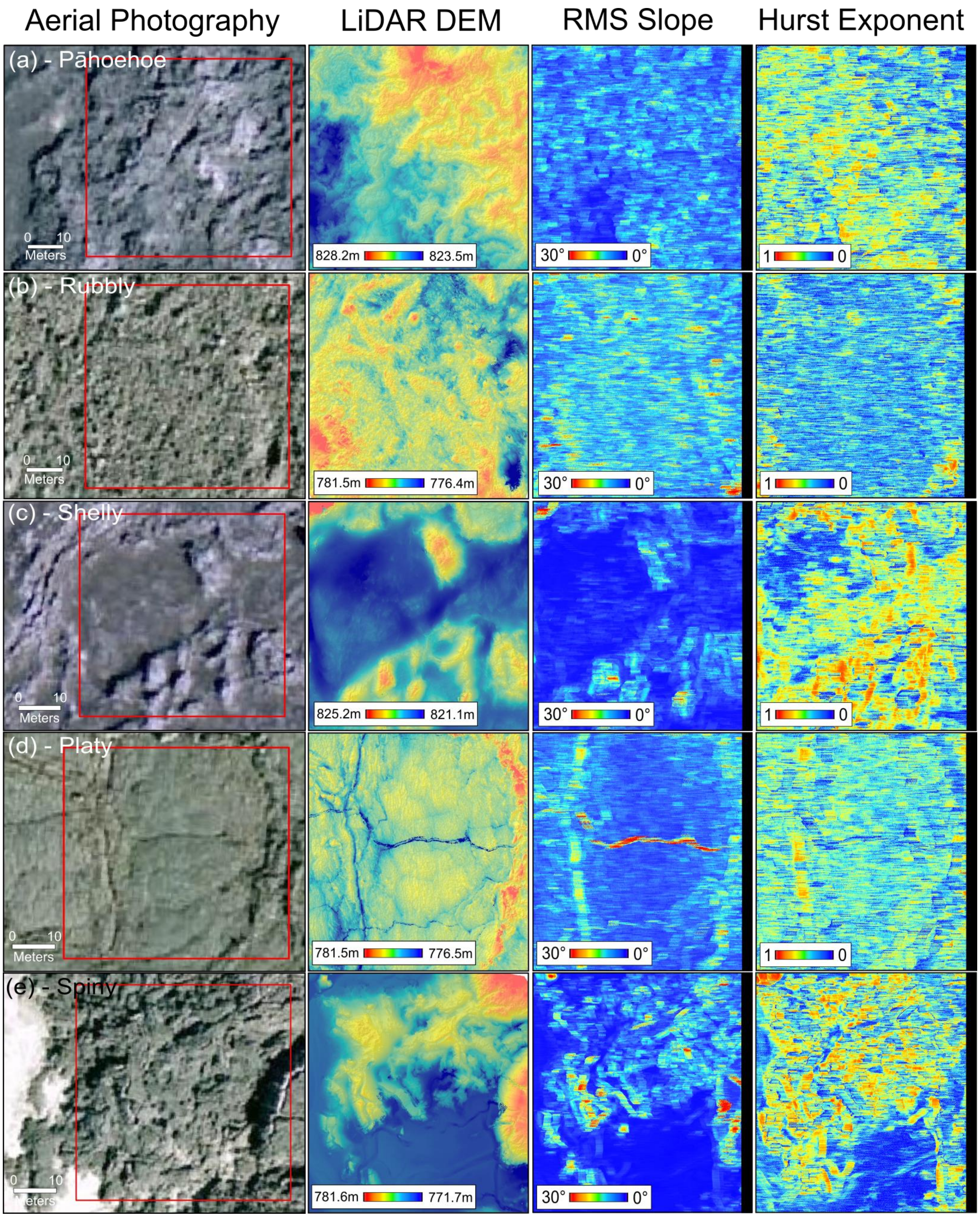

Aerial Photography
LiDAR DEM
RMS Slope
Hurst Exponent
(a) - Pāhoehoe
0 10
Meters
828.2m 823.5m
30° 0°
1 0
(b) - Rubbly
0 10
Meters
781.5m 776.4m
30° 0°
1 0
(c) - Shelly
0 10
Meters
825.2m 821.1m
30° 0°
1 0
(d) - Platy
0 10
Meters
781.5m 776.5m
30° 0°
1 0
(e) - Spiny
0 10
781.6m 771.7m
30° 0°

Figure 11. Topography and roughness data of each lava type presented in this study. The first column contains Loftmyndir.ehf aerial photography images of the lava flows, the second column shows an example of the colourized LiDAR DEMs overlying an elevation hillshade, and the third and fourth columns are the RMS slope and *H* raster's (0.05–0.25 m reference scale, 2.5 m profile) produced from the DEMs. The images represent a (a) pāhoehoe, (b) rubbly, (c) shelly, (d) platy, and (e) spiny lava type. The resolution of the DEMs are 5 cm/pixel, which allows us to view their centimetre-scale surface roughness, including pāhoehoe ropy textures, lava waves, and spiny toes. The red boxes show the boundaries of the DEMs over the Loftmyndir.ehf aerial images. The black region in the RMS slope and *H* raster's represent the last 2.5 m of the row; each pixel represents the parameters extracted from one 2.5 m profile, so we cannot obtain values for this region.

The second reference scale used for this study was 0.25–2 m (Figure 13). Compared to the centimetre-scale topographic roughness data, these surfaces have similar *H* values, from 0.2 to 0.6, and only marginally greater RMS slope values, up to 16.9°. The platy lava returned a range of RMS slope values, from 3.5° ± 0.31° to 7.6° ± 0.71°, with most RMS slope results overlapping the shelly pāhoehoe and pāhoehoe flow types. The spiny pāhoehoe and the rubbly pāhoehoe are the roughest lava surfaces at this scale (16.2° ± 1.22° and 16.9° ± 1.14°).

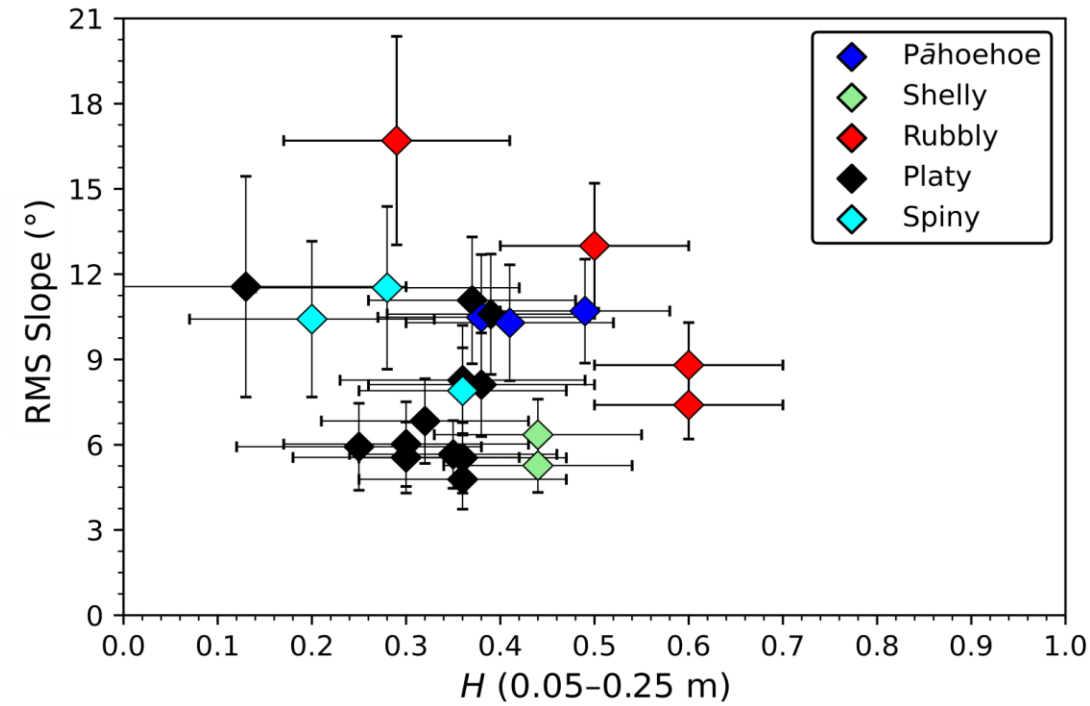

Figure 12. Centimetre-scale roughness of the studied Holuhraun lava types and subsets of the spiny pāhoehoe lava type, derived from the analysis of LiDAR DEMs with 5 cm/pixel horizontal resolution. Profile length was set to 2.5 m with a step interval of 0.05 m and a reference scale set at 0.05–0.25 m.

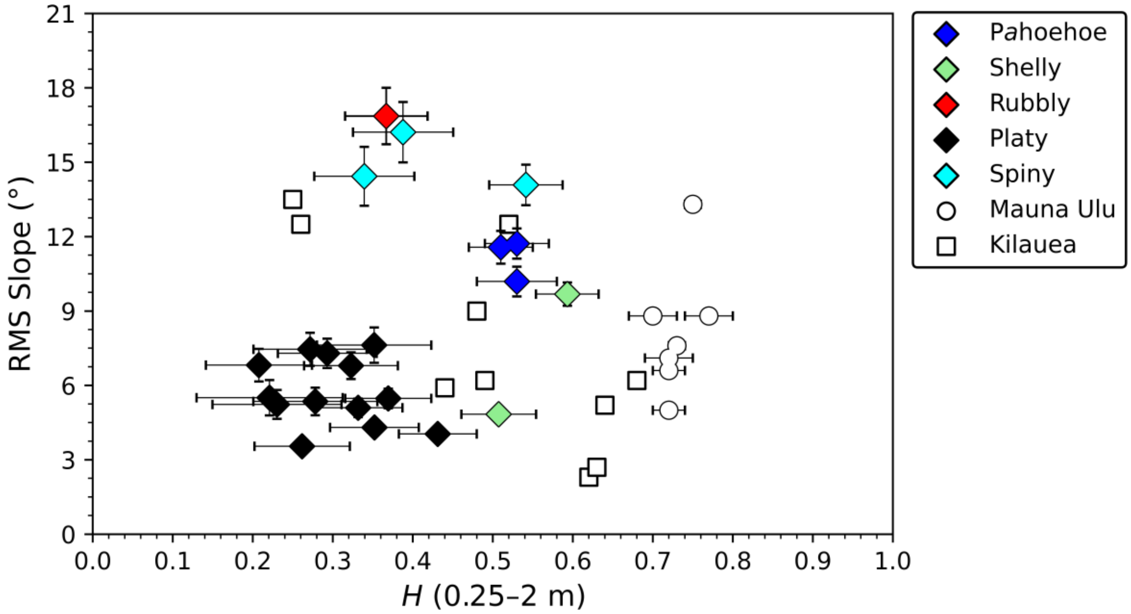

Figure 13. Decimetre-scale roughness of the studied Holuhraun lava types and subsets of the spiny pāhoehoe lava type, derived from the analysis of LiDAR DEMs with 5 cm/pixel horizontal resolution. Profile length was set to 20 m with a step interval of 25 cm and a reference scale set to 0.25–2 m. Mauna Ulu data here are reported in Neish et al. (2017) and the Kīlauea data are reported in Campbell (2002).

Table 2

RMS Slope and Hurst Exponent Measurements Calculated from LiDAR Topography Data

LiDAR Dataset	Surface Roughness	RMS Slope (°)[a]	RMS Slope Std (°)[a]	H[a]	Herr[a]	RMS Slope (°)[b]	RMS Slope Std (°)[b]	H[b]	Herr[b]
20190805_1_a	Pāhoehoe	10.29	2.04	0.41	0.11	11.6	0.66	0.50	0.04
20190805_1_b	Pāhoehoe	10.48	2.21	0.38	0.11	10.2	0.60	0.50	0.05
20190805_1_c	Pāhoehoe	10.70	1.83	0.49	0.09	11.7	0.61	0.50	0.04
20190803_1_a	Rubbly	16.70	3.67	0.29	0.12	16.9	1.14	0.40	0.05
hotsprings_a_1	Rubbly	7.40	1.20	0.60	0.10	–	–	–	–
hotsprings_a_2	Rubbly	8.80	1.50	0.60	0.10	–	–	–	–
hotsprings_a_3	Rubbly	13.00	2.20	0.50	0.10	–	–	–	–
20190801_1_b	Shelly	5.27	0.95	0.44	0.10	4.84	0.24	0.50	0.05
20190801_1_c	Shelly	6.35	1.25	0.44	0.11	9.68	0.47	0.60	0.04
20190729_2_a	Platy	11.08	2.23	0.37	0.11	6.82	0.66	0.20	0.07
20190729_2_b	Platy	10.59	2.12	0.39	0.11	7.29	0.59	0.30	0.06
20190729_2_c	Platy	4.78	1.05	0.36	0.11	3.55	0.31	0.30	0.06
20190729_2_d	Platy	5.54	1.24	0.36	0.11	4.04	0.26	0.40	0.05
20190729_2_e	Platy	5.66	1.19	0.35	0.11	5.47	0.40	0.40	0.05
20190729_3_a	Platy	6.47	1.87	0.23	0.15	5.50	0.71	0.20	0.09
20190729_3_b	Platy	5.93	1.53	0.25	0.13	5.23	0.58	0.20	0.08
20190802_1_e	Platy	11.56	3.88	0.13	0.17	7.46	0.67	0.30	0.07
20190804_1_a	Platy	6.02	1.49	0.30	0.13	7.62	0.71	0.40	0.07
20190804_1_b	Platy	6.83	1.49	0.32	0.11	5.09	0.38	0.30	0.06
20190804_1_c	Platy	8.11	1.82	0.38	0.12	6.79	0.54	0.30	0.06
20190804_2_a	Platy	5.55	1.25	0.30	0.12	4.30	0.31	0.40	0.06
20190804_3_a	Platy	8.27	1.93	0.36	0.13	5.35	0.56	0.30	0.08
20190802_1_d	Spiny	10.42	2.74	0.20	0.13	14.4	1.19	0.30	0.06
20190803_1_b	Spiny	11.52	2.86	0.28	0.14	16.2	1.22	0.40	0.06
20190803_1_c	Spiny	7.90	1.51	0.36	0.11	14.1	0.82	0.50	0.05

Note: RMS slope and H values were calculated from the LiDAR DEM data sets at 0.05–0.25 m[a] and 0.25–2 m[b] scales. Table includes RMS slope (°), Hurst Exponent (H), RMS slope standard deviation (std) (°), and Hurst exponent standard deviation (H_{std}).

In addition to the LiDAR data, we analyzed the metre-scale roughness of the three lava facies using a DEM (2 m/pixel) (Figure 14) acquired by the ArcticDEM project (Polar Geospatial Center, 2017). It has greater coverage than the LiDAR data used in this study, and although its resolution is coarser, it is more comparable to DEM data sets produced from stereo-pairs of high-resolution images of other worlds (Sutton et al., 2022), such as those taken by the Mars Reconnaissance Orbiter (MRO) High Resolution Imaging Science Experiment (HiRISE) camera (McEwen et al., 2007) and the Lunar Reconnaissance Orbiter (LRO) Narrow-Angle Camera (NAC) (Chin et al., 2007). From the ArcticDEM data, we were able to extract RMS slope and *H* values at a scale of 2–12 m (Table 3). This scale has been used by other workers to study the metre-scale roughness of terrestrial lava flows (e.g., Campbell et al., 2003), lunar impact melt flows (e.g., Neish et al., 2017), and Martian lava flows (e.g., Rodriguez-Sanchez-Vahamonde and Neish, 2021). We set the profile length to 100 m and found that the rubbly, spiny, and undifferentiated rubbly–spiny facies have RMS slope values lower than the lowest value extracted from the centimetre- and decimetre-scale data sets (Figure 15). The *H* values are also significantly greater, >0.75, implying that surface roughness will be maintained as the scale increases. RMS slope is dependent on the step size of the profile, therefore as step size increases RMS slope tends to decrease (Shepard et al., 2001). This could be one explanation as to why we observe lower RMS slope values from the 100 m profiles. Compared to other lava flows measured at the metre-scale, the 2014–2015 Holuhraun lava flow-field lava facies are considerably smoother (Figure 15, Mauna Ulu data points).

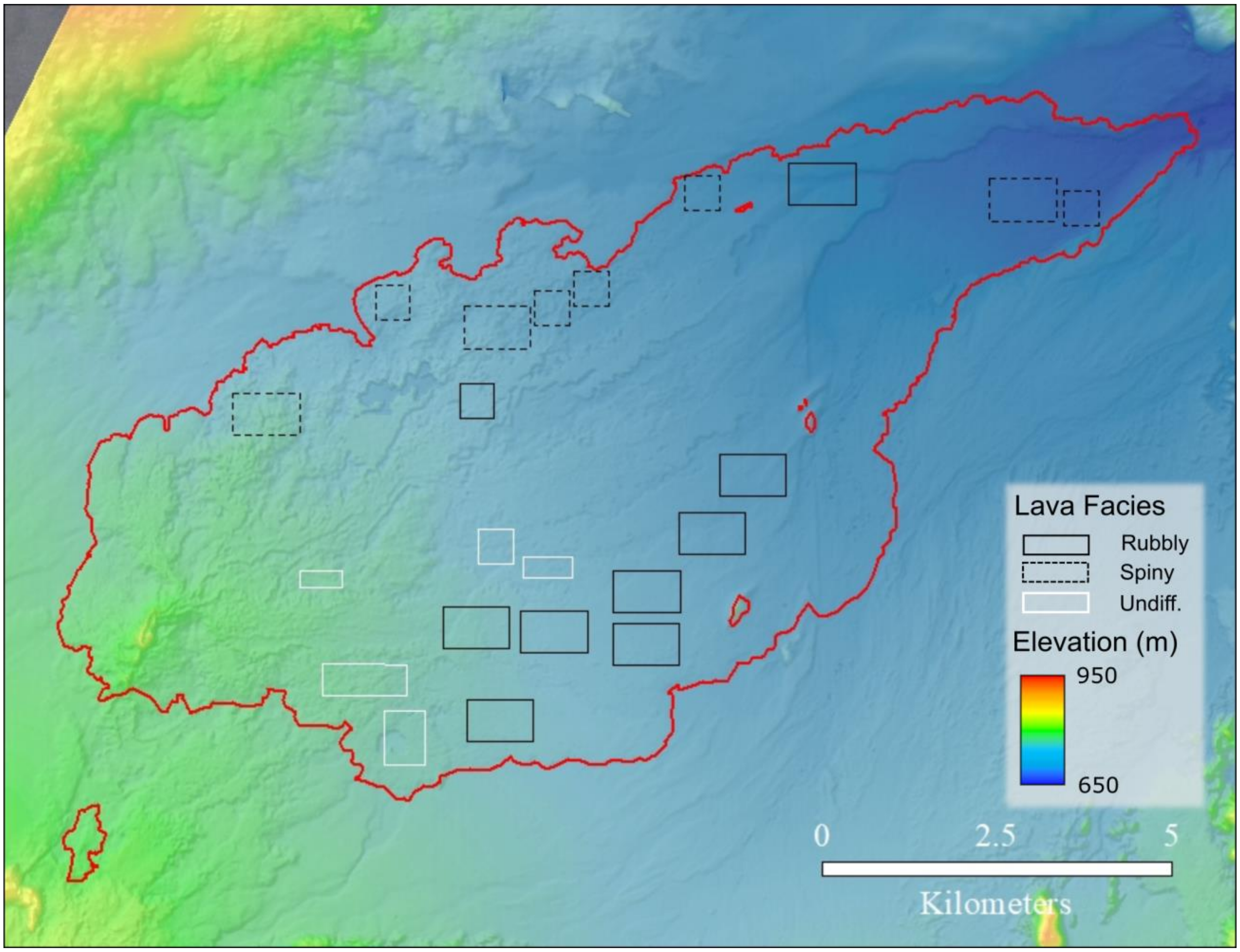

Figure 14. ArcticDEM topography data (2 m/pixel) overlaid on a colourized DEM hillshade (30° illumination angle). The black polygons represent the locations where topography data was extracted for metre-scale roughness calculations. The red polygon marks the margins of the Holuhraun lava flow-field.

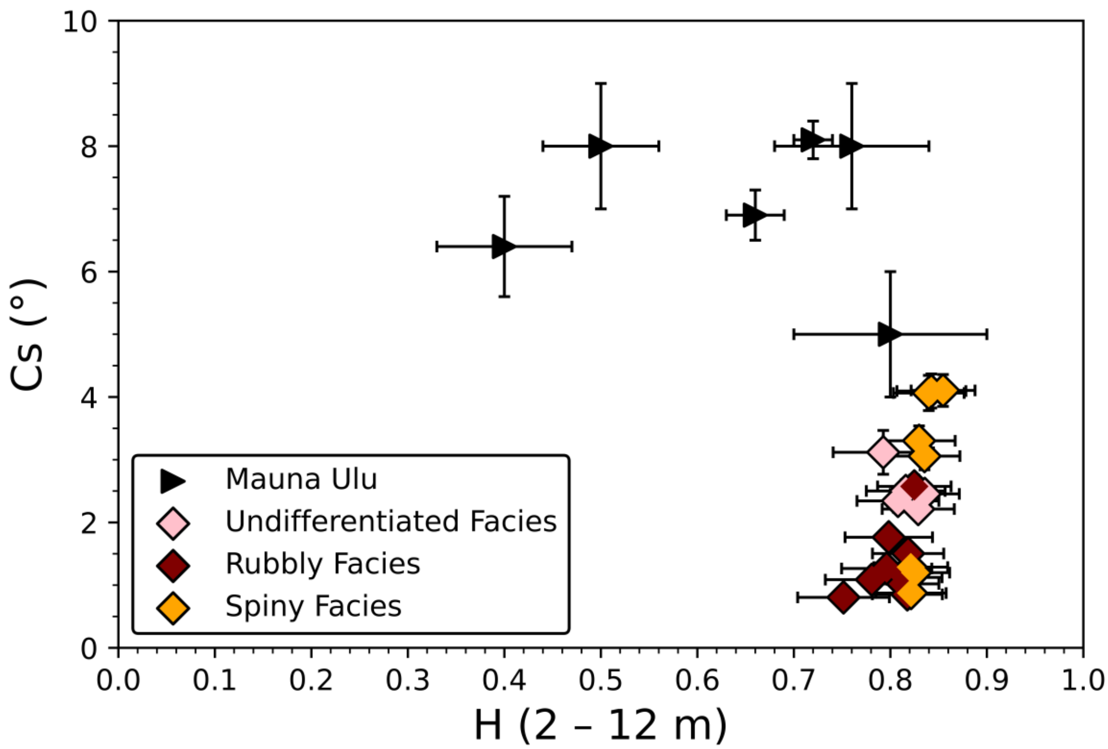

Figure 15. Metre-scale roughness of the three dominant lava facies in the 2014–2015 Holuhraun lava flow-field. The Mauna Ulu data presented here are from Hawaiian lavas reported in Campbell (2002) (Kīleaua), measured at 2–12 m reference scale and 1 m step sizes. The RMS slope and *H* were calculated from ArcticDEM data with a spatial resolution of 2 m/pixel. All of the lava facies are smooth at the metre-scale, but the rubbly facies are the smoothest (RMS slope <2.6°) out of all three. Lava facies metre-scale roughness data is summarized in Table 3.

Table 3

RMS Slope and Hurst Exponent Measurements Extracted from ArcticDEM Topography Data.

Lava Facies	RMS Slope (°)	RMS Slope Std. (°)	H	H_{std}
Rubbly	0.81	0.08	0.75	0.05
Rubbly	1.27	0.12	0.80	0.05
Rubbly	1.76	0.15	0.80	0.05
Rubbly	1.02	0.07	0.81	0.04
Rubbly	1.12	0.08	0.82	0.04
Rubbly	1.09	0.10	0.78	0.05
Rubbly	1.50	0.10	0.82	0.04
Rubbly	0.85	0.06	0.82	0.04
Rubbly	2.57	0.18	0.82	0.04
Spiny	12.95	2.55	0.73	0.07
Spiny	4.06	0.28	0.84	0.04
Spiny	3.30	0.24	0.83	0.04
Spiny	4.10	0.27	0.84	0.04
Spiny	4.10	0.25	0.85	0.03
Spiny	3.06	0.22	0.84	0.04
Spiny	1.20	0.08	0.83	0.04
Spiny	0.87	0.06	0.82	0.04
Undiff.	1.29	0.09	0.82	0.04
Undiff.	2.50	0.18	0.82	0.04
Undiff.	2.34	0.18	0.81	0.04
Undiff.	2.21	0.16	0.83	0.04
Undiff.	2.46	0.16	0.84	0.04

Note: RMS slope and H values were calculated from the ArcticDEM data set (16_54_1_2_2m_v3.0) at 2 m to 12 m. Table includes RMS slope (°), H, RMS slope std (°), and H_{std}*. The data are plotted in Figure 14.*

4 Discussion

4.1. Differentiation of Lava Facies Using Radar

Visual inspection of the CPR and VH/VV maps (Figures 9a and 10a) suggest variations over surface of the 2014–2015 Holuhraun lava flow-field that could enable automated mapping of lava facies using radar data. However, the eye is prone to finding patterns within noisy data. Examination of the CPR and VH/VV within each of the dominant facies (Figures 9b–e and 10b–2) similarly reveals some structure, but also wide variability. To determine if CPR and VH/VV values within each facies are separable in a meaningful way, first applied a Kruskal–Wallis test to determine, which, if any, facies have distinguishable radar data populations; and then we examined what proportion of each population overlap.

The Kruskal–Wallis test shows that all of the facies have medians that are distinguished from one another using CPR data and all, but the undifferentiated rubbly–spiny and spiny facies, are statistically separable using VH/VV data. However, high confidence in statistical separability of the population medians results in large part to the large samples sizes, which range from over 2×10^5 for the undifferentiated rubbly–spiny facies to over 1.0×10^6 for the rubbly facies. If one were instead to draw a single observation, or sample, it would not be possible to reliably determine the associated facies because facies populations have large overlapping radar values (Figure 8c and d). For instance, CPR values for the three main facies overlap by 88–89% and their VH/VV values overlap by 64–67% for VH/VV (Figure 8e and f). Caution is therefore urged in terms of mapping lava facies using radar or other topographic roughness data.

One reason for the large overlap among the radar populations is that the CPR and VH/VV radar data reached a saturation for ‘rough’ surface characteristics (Campbell, 2009; Campbell et al., 2003). The greater return in cross-polarized product VH in the C-band Sentinel-1 data, and moderate CPR in the L-band UAVSAR data implies that the lava facies surfaces predominantly favour diffuse (i.e., volume) scattering mechanism (Campbell, 2002; Campbell & Shepard, 1996; Carter et al., 2011; Neish & Carter, 2014). A saturation in radar data would explain why the mean CPR and VH/VV and threshold maps tend to homogenize around a narrow value range. Alternatively, the surfaces may lack features, such as smooth-facets and natural corner reflectors, which promote double-bounce scattering, which lead to increase returns in SC polarization and like-polarized data products (i.e., VV).

In the northeastern and northwestern regions of the lava flow-field (see Figure 8), the rubbly facies show a higher CPR compared to the spiny facies. However, the rubbly facies' lower CPR in the central and southern regions made it more challenging to differentiate them from the spiny facies. It is not clear why the CPR of the rubbly facies is lower in this region. For a decrease in CPR to occur, the rubbly facies in the central and southern regions must either exhibit surfaces that are more favourable for quasi-specular reflection (i.e., single-bounce; mirror-like reflection) (Neish & Carter, 2014), which is inconsistent with the scattering mechanisms typically associated with rubbly surfaces, or the size of the surface scatterers are not detectable by the UAVSAR L-band wavelength. However, the majority of the central and southern region of the lava flow-field was mapped using aerial images (Voigt et al., 2021a), and so no ground-truth data is available to differentiate between these two hypotheses.

From the VH/VV threshold map, the VH/VV data of the rubbly facies are the lower compared to the spiny facies (see Figure 9), implying that their surfaces are smoother at the centimetre-scale. This is true across the entire lava flow-field, unlike the CPR data that shows regional differences. This implies that at the centimetre-scale, the surface roughness of the rubbly facies is more consistent and shows little to no change from the vent to the end of the lava flow-field in the northeast. The variable CPR of the rubbly facies across the lava flow-field is connected to transitions in lava transport processes that occurred during the Holuhraun eruption. A change in a lava flow's surface roughness is typically connected to the emplacement style and evolution of the lava flow-fields eruption dynamics (e.g., Guilbaud et al., 2005; Harris et al., 2017; Rowland and Walker, 1990; Tolometti et al., 2020). If centimetre-scale roughness remains constant, and decimetre-scale roughness increases moving further from the vent, then it is likely that changes in lava emplacement produced more decimetre- to metre-sized surface scatterers in the northeastern and northwestern regions of the flow field.

4.2. Centimetre- to Metre-Scale Roughness of Lava Types

Our results show that with a reference scale of 0.05 m to 0.25 m and a set profile length of 2.5 m, it is difficult to separate the lava types inside the Holuhraun lava facies at the centimetre-scale. The spiny pāhoehoe, platy lava, shelly pāhoehoe, and pāhoehoe lava types all exhibit similar RMS slopes, making it challenging to identify them from topographic roughness alone. This is consistent with field observations of these lava types. All share similar volcanic surface characteristics such as spines, ropes, folds, which would contribute to the centimetre roughness, therefore the RMS slope. The rubbly pāhoehoe lava type has the greatest RMS slope (16.7°) and H overall, but exhibits significant statistical overlap with the platy, spiny pāhoehoe, and shelly pāhoehoe lava types. When we increased the reference scale (0.25 m – 2 m) and profile length (20 m), we immediately noticed a change in the distribution of RMS slope and H. The rubbly pāhoehoe and the spiny pāhoehoe are the roughest lava types at this scale, and unlike at the centimetre-scale, we do not observe significant data overlap with other lava types. From the L-band CPR and C-band VH/VV data, the lava types show no clear distinctions between each other (Figure 16). Compared with the RMS slope at both scales, the CPR and VH/VV results plateau, with the exception of some platy lava types with low RMS slope (<6°) returning higher VH/VV values creating a slightly skewed appearance. It appears that at L-band and C-band wavelengths the lava types become challenging to resolve at mappable scales. Only from the decimetre-scale LiDAR topography data do we observe differences between the lava types.

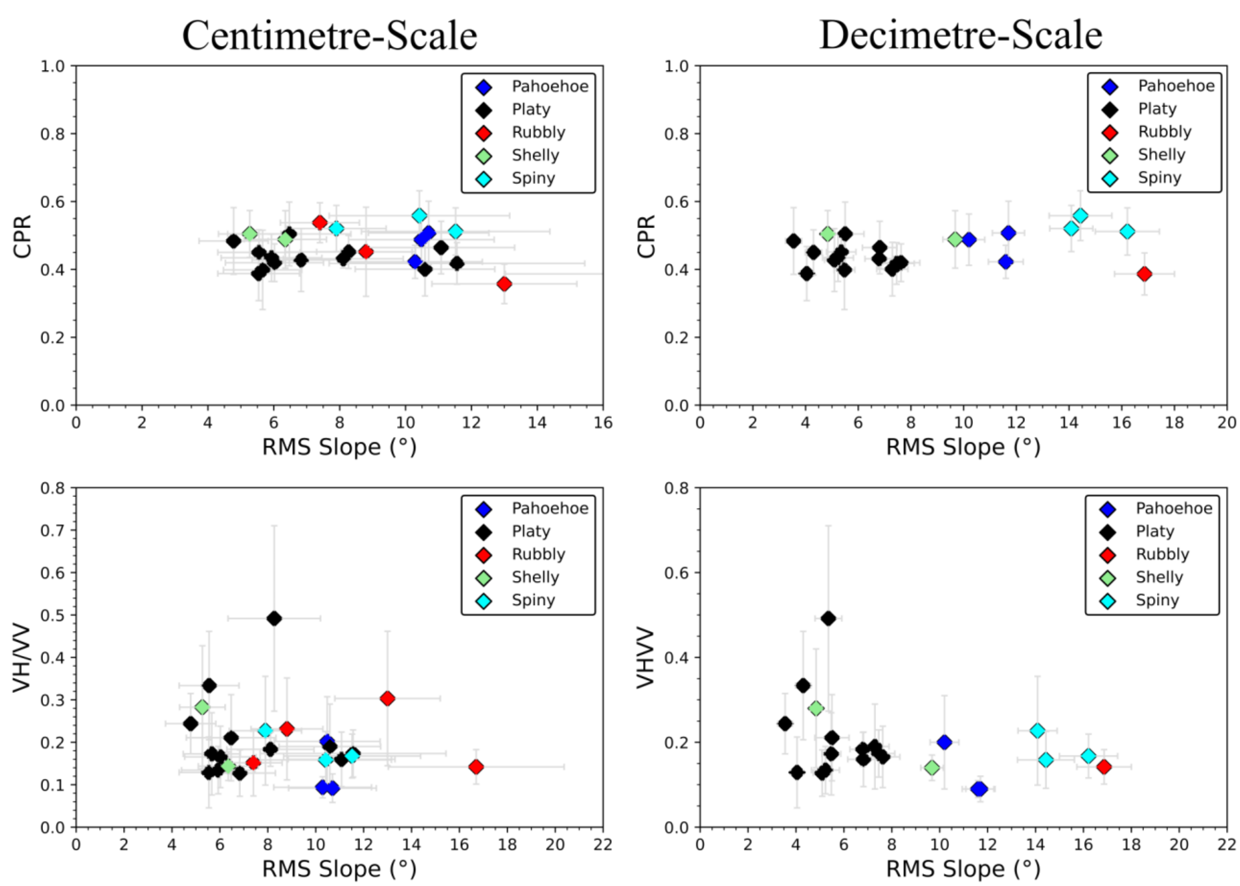

Figure 16. Comparison of Holuhraun lava type decimetre- and centimetre-scale RMS slope and L-band CPR and C-band VH/VV data. Rubbly and spiny lava types can be distinguished using RMS slope at the decimetre-scale, and quantified radar data (CPR and VH/VV) shows no clear distinctions between the lava types with the exception of VH/VV data of the platy lava type.

Overall, we find that centimetre-scale topographic roughness and radar data is not effective at discriminating different lava types and their morphological subsets, while with decimetre-scale topographic roughness we are able to separate the rubbly pāhoehoe and spiny pāhoehoe lava from the other lava types. The lack of separation is partly due to the lava facies and lava types being within the high end of the lava flow roughness spectrum, where topographic and radar backscatter signals can appear similar for different surface textures (Campbell & Shepard, 1996; Kilburn, 2000). Separation could be improved if we had access to additional radar observations acquired at different incidence angles and larger wavelengths (e.g., P-band, λ = 68 cm) (Campbell et al., 2003; Campbell & Shepard, 1996; Shepard et al., 2001); however, this was not possible for this study.

Comparing the RMS slope values of the lava types to their corresponding lava facies, we notice that the roughest lava types at the decimetre-scale (rubbly pāhoehoe and spiny pāhoehoe) are found within all three of the dominant lava facies. This could explain why we observe some similarities in the lava facies L-band CPR and C-band VH/VV results, particularly between the rubbly facies and the undifferentiated rubbly-spiny facies. The platy lava types are primarily found in the spiny facies, and their low RMS slope values at both roughness scales could be the contributing factor to the lower CPR values in the spiny facies.

5 Conclusion

Fissure-fed eruptions have highly variable effusion rates and can develop unstable lava pathways that are prone to blockages and collapses. Sudden changes in local lava fluxes can trigger the disruption and remobilization of previously solidified crust above active lava pathways, resulting in “transitional” lava types (e.g., platy, slabby, rubbly, spiny pāhoehoe). In contrast to relatively smooth pāhoehoe and rough ‘a‘ā lava type end-members, “transitional” lava types can exhibit a wider range of surface morphologies because their formation mechanisms commonly involve multiple stages of emplacement. A single flow may therefore include a mixture of surface materials that have been modified and partially overprinted at different times. At reasonable mapping scales (e.g., 1:800), surfaces may exhibit a mixture of lava types than cannot be resolved. Therefore, rather than directly mapping lava types, Voigt et al. (2021a) advocate for mapping facies units, which exhibit similar albedo, texture, and morphology. Facies units may be dominantly composed of a particular lava type—for instance, rubbly facies will primarily include the rubbly pāhoehoe; or the spiny facies will primarily include the spiny pāhoehoe), but there in an inherent recognition that most facies will also include minor exposures of other lava types.

Manual facies mapping efforts are time-intensive and subjective and so we performed an analysis to determine if the lava facies in the 2014–2015 Holuhraun lava flow-field, can be differentiated using radar and topographic measurements. First, we examined UAVSAR L-band CPR data and Sentinel-1 C-band VH/VV data for the three dominant facies mapped by Voigt et al. (2021) and then we examined surfaces at a finer scale using LiDAR to determine if topographic roughness could be further used to separate lava facies into constituent lava types.

If we consider the entire lava flow-field, the distribution of CPR and VH/VV values within each of the three major facies, they are generally all distinguishable from one another (with the exception of the VH/VV undifferentiated rubbly–spiny and VH/VV spiny facies) based on statistical separation of their population medians using the Kruskal–Wallis test. However, on a practical level, CPR values overlap by 88–89% and VH/VV values overlap by 66–67%. We therefore conclude that with a large enough sample size one could estimate the likelihood that a flow-field includes a particular facies, but not robustly determine the facies identity of any given sample.

Topographic roughness analysis of individual lava types that comprise the lava facies revealed that the rubbly pāhoehoe and spiny pāhoehoe lava types are the roughest at the decimetre-scale. At the centimetre-scale, we observed no clear differences between any of the lava types, especially between the platy lava and the spiny pāhoehoe lava type in the spiny facies. Comparing the LiDAR results to the radar data shows that all of the lava types seem to saturate around a relatively short range of CPR (~0.4 to ~0.6) but show slightly more variability in the VH/VV data. We conclude that the use of the L-band and C-band to distinguish the lava types within the rough Holuhraun lava facies is challenging, as we observe no noticeable differences that can strongly support separating them using the radar data.

Our investigation of lava types and facies using radar data has broader implications and relevance to future planetary mission concepts hosting a SAR instrument. The International Mars Ice Mapper mission concept (Davis, 2021), for example, includes an L-band SAR instrument that would be capable of measuring the surface roughness of volcanic terrains at wavelengths analogous to the UAVSAR L-band data and other terrestrial SAR platforms (e.g., ALOS PALSAR). The Mars Ice Mapper mission concept would gather vital radar backscatter and polarization data that could be used to investigate the emplacement of lava flow-fields, flood lavas, and flood basalts on Mars. In addition to Mars, the newly selected NASA Venus Emissivity, Radio Science, Insar, Topography, And Spectroscopy (VERITAS) mission (Hensley et al., 2012) and the ESA EnVision missions (Ghail et al., 2012) to Venus both have a SAR instrument. The EnVision mission will incorporate a dual-polarimetric S-band (λ = 9.4 cm) SAR instrument known as the Venus Synthetic Aperture Radar (VenSAR), which is capable of quantifying surface roughness at the decimetre-scale. New data from VenSAR will provide opportunities for comparative studies with S-band terrestrial radar data of lava flows, such as that from the NASA-ISRO SAR Mission (NISAR), which is expected to launch towards the end of 2022 (Rosen & Kumar, 2021). Based on our findings, we urge caution in trying to directly map lava facies using radar data with wavelengths between C- and L-Band because lava flows within the high roughness spectrum can exhibit morphological similarities even though they may form by different processes.

Acknowledgements

This research was funded and supported by the Canadian Space Agency Flights and Fieldwork for the Advancement of Science and Technology (FAST) program. During the field deployment at Holuhraun, work was conducted with support from P. Whelley, K. Young, J. Richardson, and the NASA Goddard Instrument Field Team (GIFT). Thanks also to E. Schaefer and C. Rodriguez Sanchez-Vahamonde for assistance in the field and LiDAR site selections. C.W.H. acknowledges support from the NASA Planetary Science and Technology from Analog Research program (Grant # 80NSSC21K0011) and Fulbright–NSF Arctic Research Scholarship program, administered by Fulbright–Iceland. Processed data presented in this research is openly available on doi:10.17632/tmpwd4gdx8.1.

References

Benjamini, Y., & Braun, H. (2002). John W. Tukey's contributions to multiple comparisons. *ETS*

Research Report Series, *2*(i–27). https://doi.org/10.1214/aos/1043351247

Bonnefoy, L. E., Hamilton, C. W., Scheidt, S. P., Duhamel, S., Höskuldsson, Jónsdottir, I., et al. (2019). Landscape evolution associated with the 2014–2015 Holuhraun eruption in Iceland. *Journal of Volcanology and Geothermal Research*, *387*, 106652. https://doi.org/10.1016/j.jvolgeores.2019.07.019

Bonny, E., Thordarson, T., Wright, R., Höskuldsson, A., & Jónsdóttir, I. (2018). The Volume of Lava Erupted During the 2014 to 2015 Eruption at Holuhraun, Iceland: A Comparison Between Satellite- and Ground-Based Measurements. *Journal of Geophysical Research: Solid Earth*, *123*(7), 5412–5426. https://doi.org/10.1029/2017JB015008

Campbell, B A. (2002). *Radar Remote Sensing of Planetary Surfaces*. Cambridge University Press.

Campbell, Bruce A. (2009). Scale-dependent surface roughness behavior and its impact on empirical models for radar backscatter. *IEEE Transactions on Geoscience and Remote Sensing*, *47*(10), 3480–3488. https://doi.org/10.1109/TGRS.2009.2022752

Campbell, Bruce A., Ghent, R. R., & Shepard, M. K. (2003). Limits on inference of Mars small-scale topography from MOLA data. *Geophysical Research Letters*, *30*(3), 1–4. https://doi.org/10.1029/2002GL016550

Campbell, Bruce A. (2012). High circular polarization ratios in radar scattering from geologic targets. *Journal of Geophysical Research*, *117*(E6). https://doi.org/10.1029/2012JE004061

Campbell, Bruce A, & Shepard, M. K. (1996). Lava flow surface roughness and depolarized radar scattering. *Journal of Geophysical Research*, *101*(E8), 18,941-18,951.

Candela, S. G., Howat, I., Noh, M. J., Porter, C. C., & Morin, P. J. (2017). ArcticDEM Validation and Accuracy Assessment. In *In AGU Fall Meeting Abstracts* (pp. C51A-0951).

Carter, L. M., Campbell, D. B., & Campbell, B. A. (2004). Impact crater related surficial deposits on Venus : Multipolarization radar observations with Arecibo. *Jounral of Geophysical Research*, *109*(E6). https://doi.org/10.1029/2003JE002227

Carter, L. M., Campbell, D. B., & Campbell, B. A. (2011). Geologic studies of planetary surfaces using radar polarimetric imaging. *Proceedings of the IEEE*, *99*(5), 770–782. https://doi.org/10.1109/JPROC.2010.2099090

Center, P. G. (2017). Polar Geospatial CenterGuide: Introduction to ArcticDEM. Retrieved December 14, 2020, from https://www.pgc.umn.edu/guides/arcticdem/introduction-to-arcticdem/

Chin, G., Brylow, S., Foote, M., Garvin, J., Kasper, J., Keller, J., et al. (2007). Lunar Reconnaissance Orbiter Overview : The Instrument Suite and Mission. *Space Science Reviews*, *129*(4), 391–419. https://doi.org/10.1007/s11214-007-9153-y

Coppola, D., Ripepe, M., Laiolo, M., & Cigolini, C. (2017). Modelling satellite-derived magma discharge to explain caldera collapse. *Geology*, *45*(6), 523–526. https://doi.org/10.1130/G38866.1

Davis, R. D. (2021). International Mars Ice Mapper Mission: The First Human Exploration Reconnaissance Mission to Mars. In *52nd Lunar and Planetary Science Conference* (p.

2614).

Dirscherl, M., & Rossi, C. (2018). Geomorphometric analysis of the 2014–2015 Bárðarbunga volcanic eruption, Iceland. *Remote Sensing of Environment*, *204*, 244–259. https://doi.org/10.1016/j.rse.2017.10.027

Duraiswami, R. A., Bondre, N. R., & Managave, S. (2008). Morphology of rubbly pahoehoe (simple) flows from the Deccan Volcanic Province: Implications for style of emplacement. *Journal of Volcanology and Geothermal Research*, *177*(4), 822–836. https://doi.org/10.1016/j.jvolgeores.2008.01.048

Duraiswami, R. A., Gadpallu, P., Shaikh, T. N., & Cardin, N. (2014). Pahoehoe-a'a transitions in the lava flow fields of the western Deccan Traps, India-implications for emplacement dynamics, flood basalt architecture and volcanic stratigraphy. *Journal of Asian Earth Sciences*, *84*(December 2015), 146–166. https://doi.org/10.1016/j.jseaes.2013.08.025

Fan, K. A., Neish, C. D., Zanetti, M., & Kukko, A. (2018). An Improved Methodology for the 3-Dimensional Characterization of Surface Roughness as Applied to Lava Flows. In *Lunar and Planetary Science Conference* (p. 2526).

Fore, A. G., Chapman, B. D., Hawkins, B. P., Hensley, S., Jones, C. E., Michel, T. R., & Muellerschoen, R. J. (2015). UAVSAR polarimetric calibration. *IEEE Transactions on Geoscience and Remote Sensing*, *53*(6), 3481–3491. https://doi.org/10.1109/TGRS.2014.2377637

Ghail, R., Wilson, C., Galand, M., Hall, D., Cochrane, C., Mason, P., et al. (2012). EnVision: taking the pulse of our twin planet. *Experimental Astronomy*, *2–3*, 337–363.

Griffiths, R. W., & Fink, J. H. (1992). The morphology of lava flows in planetary environments: Predictions from analog experiments. *Journal of Geophysical Research*, *97*(B13), 19739. https://doi.org/10.1029/92JB01953

Gudmundsson, M. T., Jonsdottir, K., Hooper, A., Holohan, E. P., Halldorsson, S. A., Ofeigsson, B. G., et al. (2016). Gradual caldera collapse at Bárdarbunga volcano, Iceland, regulated by lateral magma outflow. *Science*, *353*(6296), aaf8988. https://doi.org/10.1126/science.aaf8988.sciencemag.org

Guilbaud, M.-N., Self, S., Thordarson, T., & Blake, S. (2005). Morphology, surface structures, and emplacement of lavas produced by Laki, A.D. 1783 – 1784. *GSA Special Papers*, *396*(07), 81–102. https://doi.org/10.1130/2005.2396(07).

Hamilton, C. W. (2015). Team gets firsthand look at the new Holuhraun eruption site. *Eos*, *96*. https://doi.org/doi:10.1029/2015EO041197

Hamilton, Christopher W. (2019). *“Fill and Spill” Lava Flow Emplacement: Implications for Understanding Planetary Flood Basalt Eruptions*. *NASA Technical Memorandum: Marshall Space Flight Center Faculty Fellowship Program*.

Harris, A. J. L., Rowland, S. K., Villeneuve, N., & Thordarson, T. (2017). *Pāhoehoe, ‘a‘ā, and block lava: an illustrated history of the nomenclature*. *Bulletin of Volcanology* (Vol. 79). Bulletin of Volcanology. https://doi.org/10.1007/s00445-016-1075-7

Hensley, S., Smrekar, S. E., & Pollard, B. (2012). VERITAS: A Mission Concept for the High Resolution Topographic Mapping and Imaging of Venus. In *American Geophysical Union, Fall Meeting* (pp. P33C-1950).

Hjartardóttir, Á. R., Einarsson, P., Gudmundsson, M. T., & Högnadóttir, T. (2016). Fracture movements and graben subsidence during the 2014 Bárdarbunga dike intrusion in Iceland. *Journal of Volcanology and Geothermal Research*, *310*, 242–252. https://doi.org/10.1016/j.jvolgeores.2015.12.002

Jones, A. E. (1943). Classification of Lava-Surfaces. *Eos, Transactions American Geophysical Union*, *24*(1), 265–268.

Keszthelyi, L, Mcewen, A. S., & Thordarson, T. (2000). Terrestrial analogs and thermal models for Martian flood lavas. *Journal of Geophysical Research E: Planets*, *105*(E6), 15,027-15,049. https://doi.org/10.1029/1999je001191

Keszthelyi, Laszlo, Thordarson, T., McEwen, A., Haack, H., Guilbaud, M. N., Self, S., & Rossi, M. J. (2004). Icelandic analogs to Martian flood lavas. *Geochemistry, Geophysics, Geosystems*, *5*(11), 1–32. https://doi.org/10.1029/2004GC000758

Keszthelyi, Laszlo, Self, S., & Thordarson, T. (2006). Flood lavas on Earth, Io and Mars. *Journal of the Geological Society*, *163*(2), 253–264. https://doi.org/10.1144/0016-764904-503

Kilburn, C. R. J. (2000). Lava Flows and Flow Fields. In *Encyclopedia of Volcanoes* (pp. 291–305).

Kolzenburg, S., Jaenicke, J., Münzer, U., & Dingwell, D. B. (2018). The effect of inflation on the morphology-derived rheological parameters of lava flows and its implications for interpreting remote sensing data - A case study on the 2014/2015 eruption at Holuhraun, Iceland. *Journal of Volcanology and Geothermal Research*, *357*, 200–212.

https://doi.org/10.1016/j.jvolgeores.2018.04.024

Kolzenburg, Stephan, Giordano, D., Thordarson, T., Höskuldsson, A., & Dingwell, D. B. (2017). The rheological evolution of the 2014/2015 eruption at Holuhraun, central Iceland. *Bulletin of Volcanology*, *79*(6). https://doi.org/10.1007/s00445-017-1128-6

Lee, J.-S., & Pottier, E. (2018). Polarimetric SAR Speckle Filtering. In *Polarimetric Radar Imaging: From Basics to Applications* (pp. 143–177). https://doi.org/10.1201/9781420054989-5

López-Martínez, C., & Fàbregas, X. (2008). Model-based polarimetric SAR speckle filter. *IEEE Transactions on Geoscience and Remote Sensing*, *46*(11), 3894–3907. https://doi.org/10.1109/TGRS.2008.2002029

MacDonald, G. A. (1953). Pahoehoe, Aa, and Blocky Lava. *American Journal of Science*, *251*, 169–191. Retrieved from https://gsa.confex.com/gsa/2007AM/finalprogram/abstract_130670.htm

McEwen, A. S., Eliason, E. M., Bergstrom, J. W., Bridges, N. T., Hansen, C. J., Delamere, W. A., et al. (2007). Mars Reconnaissance Orbiter ' s High Resolution Imaging Science Experiment (HiRISE). *Jounral of Geophysical Research*, *112*(E5). https://doi.org/10.1029/2005JE002605

Minchew, B., Jones, C. E., & Holt, B. (2012). Polarimetric analysis of backscatter from the deepwater horizon oil spill using l-band synthetic aperture radar. *IEEE Transactions on Geoscience and Remote Sensing*, *50*, 3812–3830. https://doi.org/10.1109/TGRS.2012.2185804

Morris, A. R., Anderson, F. S., Mouginis-Mark, P. J., Haldemann, A. F. C., Brooks, B. A., & Foster, J. (2008). Roughness of Hawaiian volcanic terrains. *Journal of Geophysical Research E: Planets*, *113*(12). https://doi.org/10.1029/2008JE003079

Neish, C. D., Hamilton, C. W., Hughes, S. S., Nawotniak, S. K., Garry, W. B., Skok, J. R., et al. (2017). Terrestrial analogues for lunar impact melt flows. *Icarus*, *281*, 73–89. https://doi.org/10.1016/j.icarus.2016.08.008

Neish, Catherine D., & Carter, L. M. (2014). Planetary Radar. In *Encyclopedia of the Solar System* (pp. 1133–1159).

Olea, R. A. (2008). *Basic Statistical Concepts and Methods for Earth Scientists: U.S. Geological Survey*. *US Geological Survey*.

Pedersen, G. B. M., Höskuldsson, A., Dürig, T., Thordarson, T., Jónsdóttir, I., Riishuus, M. S., et al. (2017). Lava field evolution and emplacement dynamics of the 2014–2015 basaltic fissure eruption at Holuhraun, Iceland. *Journal of Volcanology and Geothermal Research*, *340*, 155–169. https://doi.org/10.1016/j.jvolgeores.2017.02.027

Rodriguez Sanchez-Vahamonde, C., & Neish, C. (2021). The Surface Texture of Martian Lava Flows as Inferred from Their Decimeter- and Meter-scale Roughness. *The Planetary Science Journal*, *2*(1). https://doi.org/https://doi.org/10.3847/PSJ/abbfac

Rosen, P. A., & Kumar, R. (2021). NASA-ISRO SAR (NISAR) Mission Status. In *IEEE Radar Conference (RadarConf21)* (pp. 1–6).

Rosen, P. A., Hensley, S., Wheeler, K., Sadowy, G., Miller, T., Shaffer, S., et al. (2006). UAVSAR: A new NASA airborne SAR system for science and technology research. In

IEEE National Radar Conference (pp. 22–29). IEEE. https://doi.org/10.1109/RADAR.2006.1631770

Rowland, S. K., & Walker, G. P. L. (1990). Pahoehoe and aa in Hawaii: volumetric flow rate controls the lava structure. *Bulletin of Volcanology*, *52*, 615–628.

Self, S., Widdowson, M., Thordarson, T., & Jay, A. E. (2006). Volatile fluxes during flood basalt eruptions and potential effects on the global environment: A Deccan perspective. *Earth and Planetary Science Letters*. https://doi.org/10.1016/j.epsl.2006.05.041

Shepard, M. K., Campbell, B. A., Bulmer, M. H., Farr, T. G., Gaddis, L. R., & Plaut, J. J. (2001). The roughness of natural terrain: A planetary and remote sensing perspective. *Journal of Geophysical Research E: Planets*, *106*(E12), 32777–32795. https://doi.org/10.1029/2000JE001429

Sigmundsson, F., Hooper, A., Hreinsdóttir, S., Vogfjörd, K. S., Ófeigsson, B. G., Heimisson, E. R., et al. (2015). Segmented lateral dyke growth in a rifting event at Bárðarbunga volcanic system, Iceland. *Nature*, *517*(7533), 191–195. https://doi.org/10.1038/nature14111

Solana, M. C., Kilburn, C. R. J., Rodriguez Badiola, E., & Aparicio, A. (2004). Fast emplacement of extensive pahoehoe flow-fields: The case of the 1736 flows from Monta??a de las Nueces, Lanzarote. *Journal of Volcanology and Geothermal Research*, *132*(2–3), 189–207. https://doi.org/10.1016/S0377-0273(03)00345-7.

Stoline, M. R. (1978). Tables of the studentized augmented range and applications to problems of multiple comparison. *Journal of the American Statistical Association*, *73*(363), 656–660. https://doi.org/10.1080/01621459.1978.10480073

Sutton, S. S., Chojnacki, M., McEwen, A. S., Kirk, R. L., Dundas, C. M., Schaefer, E. I., Conway, S. J., Diniega, S., Portyankina, G., Landis, M. E., & Baugh, N. F. (2022). Revealing Active Mars with HiRISE Digital Terrain Models. *Remote Sensing, 14(10),* 2403. https://doi.org/10.3390/rs14102403.

Thordarson, T., & Larsen, G. (2007). Volcanism in Iceland in historical time: Volcano types, eruption styles and eruptive history. *Journal of Geodynamics*, *43*(1), 118–152. https://doi.org/10.1016/j.jog.2006.09.005

Thordarson, T., & Self, S. (1993). The Laki (Skaftár Fires) and Grímsvötn eruptions in 1783-1785. *Bulletin of Volcanology*, *55*(4), 233–263. https://doi.org/10.1007/BF00624353

Tolometti, G. D., Neish, C. D., Osinski, G. R., Hughes, S. S., & Nawotniak, S. E. K. (2020). Interpretations of lava flow properties from radar remote sensing data. *Planetary and Space Science*, *190*, 104991. https://doi.org/https://doi.org/10.1016/j.pss.2020.104991

Torres, R., Snoeij, P., Geudtner, D., Bibby, D., Davidson, M., Attema, E., et al. (2012). GMES Sentinel-1 mission. *Remote Sensing of Environment*, *120*, 9–24. https://doi.org/10.1016/j.rse.2011.05.028

Voigt, J. R. C., & Hamilton, C. W. (2021). Facies map for the 2014–2015 Holuhraun eruption in Iceland. *University of Arizona, Department of Planetary Sciences, Lunar and Planetary Laboratory*.

Voigt, J. R. C., Hamilton, C. W., Scheidt, S. P., Münzer, U., Höskuldsson, Á., Jónsdottir, I., & Thordarson, T. (2021a). Geomorphological Characterization of the 2014–2015 Holuhraun Lava Flow-Field in Iceland. *Journal of Volcanology and Geothermal Research*.

https://doi.org/https://doi.org/10.1016/ j.jvolgeores.2021.107278

Voigt, J. R. C., Hamilton, C. W., Steinbrügge, G., & Scheidt, S. P. (2021b). Surface Roughness Characterization of the 2014-2015 Holuhraun Lava Flow-Field in Iceland: Implications for Facies Mapping and Remote Sensing. *Bulletin of Volcanology*.

Voigt, J. R. C., Hamilton, C. W., Steinbrügge, G., Höskuldsson, A., Jónsdottir, I., & Thordarson, T. (2021c). Linking Lava Morphologies to Effusion Rates for the 2014 – 2015 Holuhraun Lava Flow-Field , Iceland. *Geology*. https://doi.org/https://doi.org/10.1130/G49251.1

Whelley, P. L., Garry, W. B., Hamilton, C. W., & Bleacher, J. E. (2017). LiDAR-derived surface roughness signatures of basaltic lava types at the Muliwai a Pele Lava Channel , Mauna Ulu , Hawai ' i. *Bulletin of Volcanology*, *79*(11). https://doi.org/10.1007/s00445-017-1161-5

Wilson, L., & Head, J. W. (1994). Mars: Review and Analysis and of Volcanic Eruption To Theory Relationships Landforms. *Reviews of Geophysics*, *32*(3), 221–263.

Zanetti, M., Neish, C. D., Kukko, A., Choe, B.-H., Osinski, G. R., Tolometti, G. D., et al. (2018). Surface Roughness and Radar Scattering Properties of Volcanic Terrain: Geologic Application of Kinematic Mobile LiDAR Scanning. In *In Lunar and Planetary Science Conference* (Vol. 49).

Zimbelman, J. R. (1998). Emplacement of long lava flows on planetary surfaces. *J. Geophys. Res.*, *103*(B11), 27503–27516. https://doi.org/10.1029/98jb01123